Environmental Technology & Innovation 40 (2025) 104595

Contents lists available at ScienceDirect

Environmental Technology & Innovation

journal homepage: www.elsevier.com/locate/eti

Multifunctional smart polymers and citizen science for a comprehensive approach to nitrate pollution: Curative and preventive strategies

J. Lucas Vallejo-García [a], Raquel Hernández-Ruiz [a], Alba Torija-López [a], Miriam Trigo-López [a], Saturnino Ibeas [a], Laura Gómez-Cuadrado [b], Sonia Martel [b], Rocío Barros [b], Saúl Vallejos [a,*]

[a] *Grupo de Polímeros. Departamento de Química, Facultad de Ciencias, Universidad de Burgos, Plaza de Misael Bañuelos s/n, Burgos 09001, Spain*
[b] *International Research Center in Critical Raw Materials for Advanced Industrial Technologies (ICCRAM), R&D Center, Universidad de Burgos, Plaza de Misael, Bañuelos s/n, Burgos 09001, Spain*

ARTICLE INFO

Keywords:
Nitrate removal
Nitrate detection
Ion exchange polymer
Resin
Smart polymers
Water treatment
Fluorescent sensor
Toxicity assessment
Life cycle analysis (LCA)

ABSTRACT

This work presents the development and evaluation of a multifunctional smart polymer (FNO_3) for the extraction and detection of nitrates in drinking water. A total of 250 tap water samples from various localities were analyzed, revealing nitrate concentrations that in some cases doubled the legal limit (up to 100 $mg{\cdot}L^{-1}$). FNO_3, composed of 49.75 mol% NNZA monomer with high anion-exchange capacity, exhibited a maximum nitrate adsorption capacity (*qmax*) of 164 ± 5 $mg{\cdot}g^{-1}$, which is 3.6 times greater than that of commercial resins. The polymer demonstrated significant swelling in water (~2014 ± 152 %) and incorporated a sensing functionality via a fluorometric monomer, enabling visual detection when saturation occurs. Fluorescence response studies yielded a limit of detection (*LOD*) of 4.26 $mg{\cdot}L^{-1}$ and a limit of quantification (*LOQ*) of 12.92 $mg{\cdot}L^{-1}$, values that are below the regulatory thresholds established by European and Spanish legislation for nitrates in drinking water. The material was tested through multiple adsorption-regeneration cycles using domestic saline solutions, maintaining stable efficiency. Interference studies indicated that carbonates present in hard water partially reduce adsorption effectiveness. *Life Cycle Assessment (LCA)* identified the structural materials and functional monomers as the main contributors to environmental impact, while reuse and polymer application offer environmental benefits due to nitrate recovery. Additionally, in vitro toxicological assays with *HepG2* cells confirmed the absence of cytotoxicity, supporting the polymer's viability for safe water treatment applications.

1. Introduction

Nitrate pollution, mainly caused by the overuse of fertilizers and poor management of organic waste, represents a growing threat to ecosystems, human health, and climate stability (Ward et al., 2018). Nitrogen-rich compounds, particularly nitrates, infiltrate water bodies and soils through agricultural runoff, untreated sewage, and livestock waste. Once in the environment, these pollutants trigger a

---

* Corresponding author.
E-mail address: svallejos@ubu.es (S. Vallejos).

https://doi.org/10.1016/j.eti.2025.104595
Received 16 July 2025; Received in revised form 23 October 2025; Accepted 27 October 2025

cascade of harmful effects.

In aquatic ecosystems, elevated nitrate levels lead to eutrophication, promoting algal blooms that deplete oxygen, kill fish, and reduce biodiversity. On land, nitrates disrupt nutrient cycles and plant communities. Human health is also at risk: high nitrate concentrations in drinking water are associated with methemoglobinemia (or "blue baby syndrome") in infants (Majumdar, 2003), and potentially with an increased risk of certain cancers in adults (Donat-Vargas et al., 2023; Jacobsen et al., 2024). Furthermore, nitrate pollution contributes to the emission of nitrous oxide, a potent greenhouse gas, aggravating climate change.

Despite its severity, monitoring nitrate pollution remains a major challenge. Current monitoring systems are fragmented, producing low-resolution data and leaving many rural and agricultural areas without coverage. This lack of reliable data hinders effective policymaking and the implementation of targeted interventions. Global institutions such as the UN Water Conference and UNEP have emphasized the urgent need for improved water quality data to track progress toward Sustainable Development Goal 6.3.2. Although tools like the SDG Water Quality Hub attempt to consolidate existing information ("Water and Sanitation-United Nations Sustainable Development, 2025"), major gaps in availability and comparability persist.

To help address these gaps, this work explores a citizen science approach from a preventive perspective. This initiative has had significant public impact, with dozens of appearances in national media, reflecting growing social concern and awareness about nitrate pollution in rural environments (Mediaset, 2025a, 2025b).

However, monitoring alone is not enough—access to safe drinking water remains a fundamental right, as recognized in Spanish law (Law 7/1985, Art. 26) (Spain. Head of State, 1985). Yet, our study found evidence that this right is not being fulfilled in several municipalities, where nitrate levels exceed safe limits.

Current curative technologies, such as reverse osmosis and ion-exchange resins, are widely used to remove nitrates from drinking water, especially in domestic systems. However, these methods are non-selective, removing beneficial minerals alongside nitrates, often requiring post-treatment remineralization. More critically, they are wasteful and unsustainable: reverse osmosis can waste up to 10 litres of water for every litre purified, and both systems generate secondary waste streams and demand high operational costs, making them unsuitable for rural or small-scale applications.

To overcome these limitations, this study presents a novel solution: the use of reusable smart polymer materials for decentralized nitrate removal. Our material (FNO_3) consists in functionalized polymeric films capable of removing nitrates from water with high affinity under typical conditions, showing a preferential interaction with nitrate ions over other common anions such as bicarbonate anions. Once saturated, the films could be returned through a subscription service, where the captured nitrates would be recovered and reused as fertilizer in local agricultural businesses, embedding circularity into the process. Moreover, these smart materials are multifunctional; in addition to removing nitrates, they emit a fluorescent signal upon saturation, indicating the need for regeneration and thereby facilitating their use by non-specialized personnel. Thus, the smart material proposed in this work meets both classifications established by García Pérez et al. (2022), namely, it functions as both a reactive polymer and a sensory polymer.

In recent years, a specific class of polymer-based smart materials—unsupported thin films, meaning films that are not applied onto inert substrates but rather constitute the final functional material themselves—have emerged as promising tools in a wide range of applications (García Pérez et al., 2024), including biomedicine (Arnaiz et al., 2025, 2023), food safety (Gaona-Ruiz et al., 2024; Vallejo-García et al., 2023), and, as explored in this work, environmental monitoring (Bustamante et al., 2019; Guembe-García et al., 2024). These materials are synthesized via random radical polymerization directly within the final mold, differing from conventional thin films often fabricated by casting or spin-coating techniques. A key feature of this approach is that no external additives are used during synthesis: all reagents are monomers, crosslinkers, or initiators that become covalently integrated into the main polymer backbone. This additive-free composition minimizes the risk of chemical leaching, which is particularly relevant for water-contact or food-contact applications. Furthermore, the random arrangement of polymer chains has been shown to enhance performance, often surpassing that of traditional small-molecule colorimetric or fluorometric probes.

To the best of our knowledge, this material represents a significant innovation, as it operates without the need for electricity (Jobgen et al., 2007; Lin et al., 2007), specialized equipment (Jobgen et al., 2007; Miranda et al., 2001), or electrodes (Badea et al., 2001; Hutchins and Bachas, 1995)—unlike other methods and materials reported in the scientific literature. Another key distinguishing feature is that the fluorescence-switching reaction is reversible, in contrast to many commercial nitrate-detection test strips, which typically rely on irreversible diazonium coupling reactions ("Nitrate Test Strips, colorimetric 10–500 mg/L (NO3-), MQuant®, for use with MQuant® StripScan App | Sigma-Aldrich," 2025). Furthermore, the material itself integrates visual detection capability with effective nitrate removal from water, which, to the best of our knowledge, makes it a unique solution within its category.

This approach merges advanced materials science with citizen-centered design, creating a low-cost, scalable, and sustainable alternative to traditional water treatment systems. By integrating community monitoring with decentralized, circular purification technology, our material offers a holistic response to the challenges of nitrate pollution—empowering local action while supporting environmental and economic resilience.

Based on the context described above, the specific objectives of this work are: (i) to develop a multifunctional polymeric thin-film material (FNO_3) capable of selectively removing nitrates from water while providing a visual fluorescence signal for saturation detection; (ii) to evaluate the material's performance in terms of nitrate extraction efficiency, selectivity, reusability, and limits of detection and quantification under laboratory and realistic conditions; (iii) to implement a citizen science approach for monitoring nitrate pollution, assessing public engagement, and promoting awareness and preventive action in rural communities; (iv) to assess the sustainability and potential environmental impact of the proposed material through preliminary *Life Cycle Assessment (LCA)* and toxicological evaluation, ensuring the proposed solution is environmentally safe and scalable.

2. Experimental

2.1. Materials

All materials and solvents were commercially available and used as received unless otherwise indicated. The following materials and solvents were used: 1-vinyl-2-pyrrolidone (VP) (Acros Organic, 99 %), methylmethacrylate (MMA) (Merck, 99 %), 5-bromopentene (TCI, 95 %), 6-methoxyquinoline (Thermo Scientific, 98 %), methanol (VWR, 99.8 %), diethyl ether (VWR, 99.7 %), (vinylbenzyl) trimethylammonium chloride (NNZA) (Sigma-Aldrich, 99 %), hydrochloric acid (VWR, 37 %), chloroform (VWR, 99 %), ethylene glycol dimethacrylate (E) (Aldrich, 98 %), 2,2-Dimethoxy-2-phenyl-acetophenone (Aldrich, 99 %), potassium chloride (Sigma-Aldrich 99.5 %), potassium nitrate (VWR, 99.7 %), sodium carbonate (Sigma-Aldrich, 99.9 %), nitrate exchange commercial resin (Dupla, Duresin N 80563).

2.2. Instrumentation and general methods

The water-swelling percentage (WSP) of the films, defined as the percentage of water absorbed by the films upon immersion in pure water at 20 °C until equilibrium, was determined using the dry film weight (ωd) and its water-swelled weight (ωs) with the Eq. (1):

$$\mathrm{WSP} = 100 \times [(\omega s - \omega d)/\omega d] \tag{1}$$

The thermal behaviour of the polymers was analyzed using thermogravimetric analysis (TGA) performed on a Q50 TGA analyser (TA Instruments, New Castle, DE, USA) with 10–15 mg of sample under synthetic air and nitrogen atmospheres at a heating rate of 10 $^{\circ}\mathrm{C}\cdot\mathrm{min}^{-1}$.

Fourier-transform infrared (FTIR) spectra were recorded using an FT/IR-4200 infrared spectrometer (Jasco, Tokyo, Japan) equipped with an ATR-PRO410-S single-reflection accessory.

Differential scanning calorimetry (DSC) was carried out using a TA Instruments Q200 DSC analyser with a heating rate of 20 $^{\circ}\mathrm{C}\cdot\mathrm{min}^{-1}$ under a nitrogen atmosphere and 10–15 mg of sample.

^{1}H and ^{13}C{1 H} NMR spectra (Advance III HD spectrometer, Bruker Corporation, Billerica, Massachusetts, USA) were recorded at 300 MHz for 1 H and 75 MHz for 13 C using deuterated dimethylsulfoxide (DMSO-d_6) at 25 °C as the solvent.

The limit of detection (*LOD*) and the limit of quantification (*LOQ*) were estimated using the Eqs. (2) and (3):

$$\mathrm{LOD} = 3.3 \times SD/s \tag{2}$$

$$\mathrm{LOQ} = 10 \times SD/s \tag{3}$$

where *SD* is the standard deviation of a blank sample and s is the slope of the calibration curve in a region of low nitrate content.

2.3. Tap water sampling through citizen science

This study combined a large-scale citizen science initiative with a year-long intensive monitoring campaign in two selected towns. The citizen science component involved the collection of 557 water samples from multiple locations across the province of Burgos, Spain, covering an area of 14,022 km^2, and representing diverse water sources and towns. These sources included streams, springs, and other natural bodies; however, the primary focus was on tap water samples, as they are most relevant for evaluating nitrate exposure in domestic contexts. Tap water corresponds to treated water supplies—most commonly disinfected with sodium hypochlorite—whereas natural sources (springs, streams, rivers) are untreated. This focus also responds to the current Spanish regulation (Royal Decree No. 3/2023), which only applies to drinking water; natural sources such as rivers, springs, or streams fall outside the scope of the law, as they are not directly considered for human consumption. Nevertheless, given the high level of public concern, we also analyzed non-regulated natural sources (springs, streams, rivers), and these additional results—showing even higher incidences of non-compliance—are provided in the Supplementary Material (SM-Section S1).

Of the total, 250 valid tap water samples were collected from different municipalities. It is worth noting that many of the analyzed samples were duplicates originating from the same locality, and numerous others had to be discarded due to non-compliance with the sampling protocol established by our research group.

In parallel, a year-long monitoring program was conducted in the towns of Briviesca and Avellanosa del Páramo. Samples were collected approximately every four weeks throughout 2024 to capture temporal variability in tap water quality. While full experimental details are provided in SM-Section S1, a summary of the sampling approach is presented below.

For both components, the sampling protocol was simple and accessible. Participants were instructed to use a sterile sampling container or, alternatively, a standard 500 mL plastic bottle originally intended for mineral water. If using a plastic bottle, it had to be emptied and not drunk from directly. The container was to be rinsed three times with tap water from the participant's home to minimize contamination and then filled completely. The only identifying information provided with each sample was the name of the town where it had been collected.

Once collected, the samples were delivered to our laboratory facilities, where they were analyzed as described in the following sections. The results of the analyses were subsequently communicated to the corresponding local municipalities via their official institutional email addresses.

2.4. Quantification of nitrate in water samples

The determination of nitrate concentration in real water samples was carried out using UV spectrophotometry at 220 nm (Hitachi U-3900 UV/Vis spectrophotometer (Hitachi High-Tech, Japan), following the general guidelines of the Standard Methods for the Examination of Water and Wastewater (Method 4500-NO_3^- B), with specific adaptations detailed in SM-Section S2.

2.5. Design of the multifunctional smart polymer

The citizen science project not only highlighted the scope of the nitrate contamination problem but also provided insight into

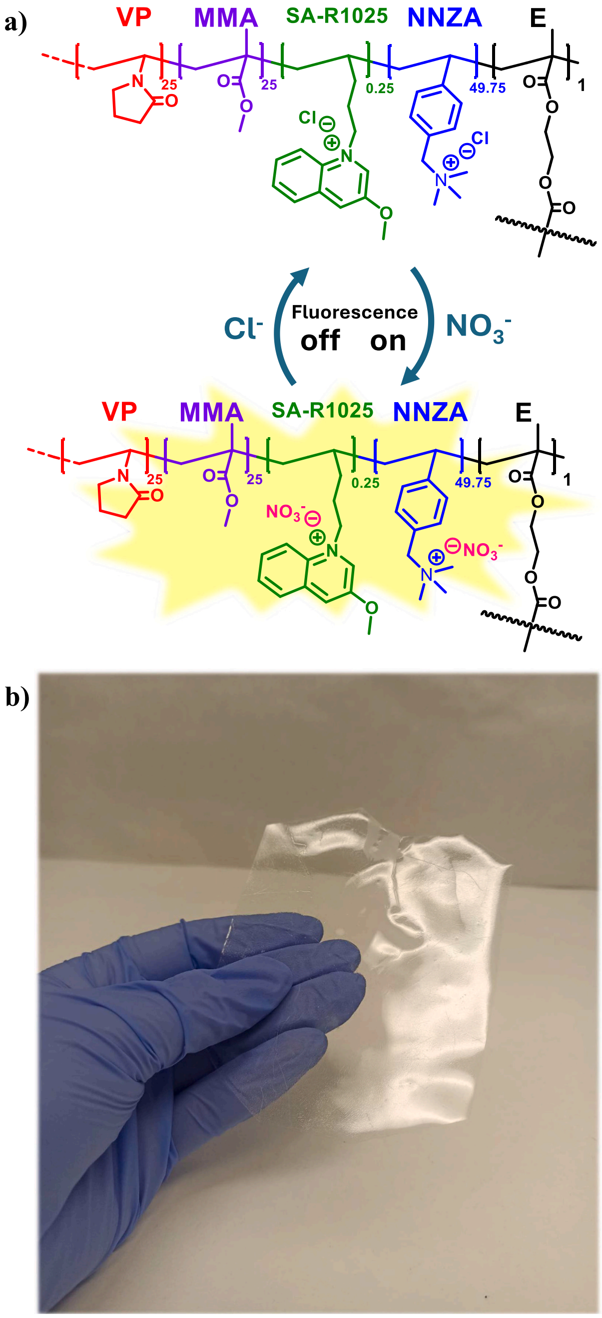

Fig. 1. a) Chemical structure of the multifunctional smart copolymer designed for nitrate removal, composed of 49.75 mol% NNZA units (anion-exchange sites), 25 mol% VP (hydrophilic component), 25 mol% MMA (providing hydrophobic rigidity), and 0.25 mol% SA-R1025 (fluorescent sensor unit). b) The photograph shows the final material (FNO_3) in its film-like format.

current solutions and the specific demands of the public regarding feasible technologies. From this, we identified key limitations in the two most commonly used household systems: reverse osmosis and ion exchange units.

While reverse osmosis systems are compact and easily installable, they often produce wastewater and can be expensive to maintain. Ion exchange resins, on the other hand, are expensive, but robust and durable, and can be regenerated with relatively simple procedures. Our approach therefore aimed to combine the advantages of both strategies.

We developed a smart material (FNO_3) inspired by the chemistry of ion exchange resins, incorporating a high proportion of NNZA-based moieties (49.75 mol%) into its structure to ensure high anion-exchange capacity (Fig. 1). To render the polymer structurally manageable and compatible with everyday use, we selected a formulation including hydrophilic N-vinylpyrrolidone (VP, 25 mol%) and hydrophobic methyl methacrylate (MMA, 25 mol%).

This balance, combined with the use of an appropriate cross-linker, resulted in a robust and easy-to-handle material, despite its high water swelling %, which reaches approximately 2014 ± 152 %, relatively high for this type of materials designed for environmental control applications (Bustamante et al., 2019) (more information about the synthesis and characterization of the polymer FNO_3 can be found in SM-Section S3).

To facilitate public engagement and use, FNO_3 was designed as a simple, immersible film that passively extracts nitrate from water. A key concern, however, was user feedback—how can users know when the film needs to be replaced or regenerated? To address this, we incorporated a small fraction (0.25 mol%) of the SA-R1025 monomer, a fluorometric sensor responsive to chloride anions (Vallejos et al., 2018) (more information about the synthesis of the monomer in SM-Section S4). The underlying sensing mechanism relies on dynamic quenching: when the polymer is in its fresh state, the NNZA sites are paired with chloride counterions that quench the fluorescence of the quinolinium core in SA-R1025. As nitrate ions replace chloride ions during the exchange process, quenching decreases and fluorescence re-emerges. This visual signal provides a straightforward and user-friendly indicator that the film has reached saturation and should be replaced or regenerated via immersion in a KCl solution.

2.6. *Sorption study*

The adsorption kinetics were monitored using absorbance measurements. Specifically, the decrease in nitrate concentration over time was tracked upon immersion of FNO_3 in the solution. To determine nitrate concentration at each time point, a calibration curve was established based on absorbance readings.

11 potassium nitrate (KNO_3) solutions were prepared, with nitrate anion concentrations ranging from 5 to 100 ppm using stock solutions prepared in Section 2.4. In this case, a wavelength of 222 nm was selected, ensuring that absorbance saturation did not occur at any concentration. All measurements were performed using a quartz cuvette filled with 3.5 mL of each solution. A 10 mm diameter disc (1.6 mg), obtained by punching directly from the polymer film, was introduced into the cuvette, and nitrate removal was monitored at 25 °C over a period of 500 min. Each concentration was tested in triplicate.

Using the obtained values of q_e (milligrams of adsorbate adsorbed per gram of adsorbent at equilibrium) and C_e (concentration of adsorbate remaining in solution at equilibrium), from the different adsorption kinetics, the adsorption isotherm was constructed by averaging these values across the three replicates performed for each concentration.

2.7. *Fluorescence and interference study*

To investigate the sensory behavior, the fluorescence enhancement of FNO_3 was monitored over time at different nitrate concentrations (50–500 ppm, in MQ water) using a Hitachi F-7000 fluorescence spectrophotometer (Hitachi, Tokyo, Japan). The procedure followed a method analogous to that used in the kinetic study, maintaining the same solution volume, amount of FNO_3, and experiment time.

Interference study: drinking water contains various dissolved salts, predominantly calcium and magnesium salts, which contribute to different degrees of water hardness. Hardness is commonly expressed in mg·L^{-1} of sodium carbonate. Accordingly, five different carbonate concentrations (50, 100, 200, 300 and 500 ppm) were prepared in MQ water to study the removal of nitrates —initially at 95 ppm— by UV-Vis spectrometry before and after the treatment with FNO_3. The experiments were conducted using a solution volume of 3.5 mL and 1.6 mg of FNO_3.

Fluorescence images of FNO_3 shown throughout the article were taken with an iPhone 16 under ultraviolet light irradiation at 365 nm.

2.8. *Reusability study*

In this study, a procedure analogous to that used in adsorption isotherm analysis (Section 2.6) was followed to evaluate the reusability of FNO_3, designed for nitrate extraction from drinking water (500 min, 25 °C). A fixed amount of 1.6 mg of FNO_3 was employed with a final volume of 3.5 mL of polluted water.

The water originated from Avellanosa del Páramo (Spain), and its salt composition was determined through external analysis conducted by the company *DXD Soluciones Químicas S.L.* Absorbance measurements of the water were taken before and after the addition of FNO_3 to quantify the extraction of nitrates and other ions present. To prevent measurement interference from carbonates, hydrochloric acid (HCl) was added after treatment with FNO_3, and prior to UV-Vis analysis.

The adsorption process was carried out for a minimum of 500 min to ensure equilibrium. Subsequently, FNO_3 was regenerated by immersing it in a 500 mg·L^{-1} potassium chloride solution for 120 min. After regeneration, FNO_3 was reused for a new purification cycle, repeating the process for a total of seven cycles.

2.9. Life cycle assessment study

This study employs a *LCA* to evaluate the environmental performance of a nitrate removal film for drinking water, considering both production and operational use phases. The functional unit is defined as 1 m^3 of treated water, enabling comparison with equivalent technologies.

The assessment was conducted following the Environmental Footprint 3.1 (EF 3.1) methodology, in accordance with ISO 14040 and ISO 14044 standards and the European Commission's recommendations (2013/179/EU). This method integrates classification, characterization, normalization, and weighting steps to derive a single environmental impact score.

The analysis comprises two stages: **Production**: synthesis of functional monomers (NNZA, SA-1025); use of polymers and additives (EGDMA, MMA, VP, DMPA); structural materials (glass, stainless steel, polyethylene); energy consumption; transportation; emissions; industrial waste; and water use. Final disposal is excluded. **Use**: transportation to the point of consumption; water consumption for regeneration; valorization of nitrate-rich effluent as fertilizer (modelled as an avoided product); and minor waste generation (plastics, syringes). End-of-life management will be evaluated in a subsequent study.

Inventory data were obtained from experiments, literature sources, and the Ecoinvent v3.8 database using a "cut-off" allocation approach. For monomers unavailable in the database, specific processes were modelled according to synthesis routes, estimating emissions and by-products by analogy.

Impact assessment was performed using SimaPro v10.2.0.1, considering categories such as climate change, human toxicity, aquatic ecotoxicity, acidification, and use of mineral and fossil resources.

2.10. Toxicology study

2.10.1. Cell line and culture conditions

The human hepatocellular carcinoma epithelial-like cell line (HepG2) was cultured in Eaglés Minimum Essential Medium (EMEM), which was prepared as follows: commercial Minimum Essential Medium (MEM) supplemented with 10 % fetal bovine serum (FBS), 1 % penicillin-streptomycin, 1 % non-essential amino acids (NEAA), and 1 % sodium pyruvate (Gibco). The cell culture was kept in a thermostatic incubator under optimal growth conditions (humidified atmosphere containing 5 % CO_2 and 37 °C).

2.10.2. Cell viability toxicology assay

- Water samples preparation

  The developed material FNO_3 was used to treat a real water sample unsuitable for human consumption, collected from Avellanosa del Páramo (Spain). The water's toxicological profile was assessed both before and after exposure to the film. The potential of the water samples—WA (untreated Avellanosa water) and WA+C (Avellanosa water exposed to the film)—to affect cell viability was evaluated using HepG2 cells exposed to the maximum concentrations of each sample, which corresponds to 90 % of the final volume.

  Prior to testing, water samples were filtered using 0.22 μm PES filters. Subsequently, the culture medium, prepared at a 10X concentration, was diluted directly into the water samples to conduct the various assays.
- MTT Assay

  HepG2 cells were seeded in 96-well plates at 1 × 104 cells per well and incubated for 24 h. Cells were washed with Phosphate-Buffered Saline (PBS) and then treated with 200 μL of the maximum water concentration diluted in culture medium supplemented as explained above. As controls, cells incubated with culture medium alone (NC = live cells control) and cells treated with water only (PC = dead cells control) were used. 24 h after exposure, the culture medium containing FNO_3 was withdrawn, and cells were washed with PBS, and then 100 μL of a solution of MTT (3-(4,5-dimethylthiazol-2-yl)-(2,5-diphenyltetrazolium bromide) (Sigma) at 500 $mg \cdot L^{-1}$ using no-supplemented culture media were added to each well, and incubated for 3 h, protecting cells from the light. After this time, the solution medium was discarded, and 100 μL of dimethyl sulfoxide (DMSO) were added per well to solubilize the formazan crystals by gentle shaking for 15 min at 500 rpm at room temperature, keeping the plate protected from light. Finally, the absorbance was measured using a BioTek Synergy HT microplate reader (BioTek Instruments, Winooski, VT, USA) at OD 590 nm. Data represent the mean of three biological replicates, each with four technical replicates (Mosmann, 1983).
- Statistical analysis

  The background absorbance was subtracted, and the values were normalized to the mean of the negative control, which is set to 100 % viability. Statistical analysis data are presented as means ± *SD*. The Two-way analysis of variance (ANOVA) was used for Dunnett́s multiple comparison test to compare every mean with the negative control sample, which is used as the internal water control sample nitrate-free. Statistical tests were carried out using Prism 8.0 (GraphPad Prism, GraphPad Software, Inc.). Differences were considered significant at $P < 0{,}05$. **** $P < 0{,}0001$.

3. Results and discussion

3.1. Results of nitrate monitoring in tap water through citizen science

Among the 250 valid samples analyzed (Fig. 2a), 22 % exceeded the maximum allowable nitrate concentration in drinking water, as established by Spanish and European regulations (50 mg·L^{-1}), which, under these standards, is classified as a "very severe" condition (European Parliament and the Council of the European Union, 2020; Ministry of the Presidency, 2023). Additionally, 30 % of the samples presented concentrations above 30 mg·L^{-1} , a threshold considered "severe" that, according to Royal Decree No. 3/2023 (Ministry of the Presidency, 2023), may trigger a correction factor if the situation persists or worsens over time. Particularly concerning is the fact that many of the affected municipalities were unaware of the problem: neither the residents nor, apparently, the local authorities had prior knowledge of the water quality issues. This lack of information and awareness on the part of the administration highlights the urgent need to implement both corrective and preventive measures.

Furthermore, various scientific studies have already pointed out that the legal limit may be too lenient. Evidence suggests that concentrations above 10 mg·L^{-1} may pose health risks, particularly in relation to colorectal and prostate cancers (Donat-Vargas et al., 2023; Jacobsen et al., 2024). Based on this more conservative threshold, 48 % of the monitored towns would be considered to have unsafe nitrate levels.

The results were sent via email to the respective municipal governments. In many cases, officials expressed surprise, as this was the first time they had been alerted to the issue. Contrary to the assumption that this is a problem limited to small, depopulated rural villages—where limited municipal resources might explain the lack of oversight—this is not always the case. For instance, a sample provided by a citizen from Aranda de Duero, the third most populous city in the province of Burgos, revealed a nitrate concentration of 58 mg·L^{-1}, exceeding the legal limit. This result was rapidly communicated to the local authorities and confirmed with a second analysis, highlighting that the currently available platforms for checking nitrate concentrations in water need improvement, and that the communication of these results to citizens should also be made more effective.

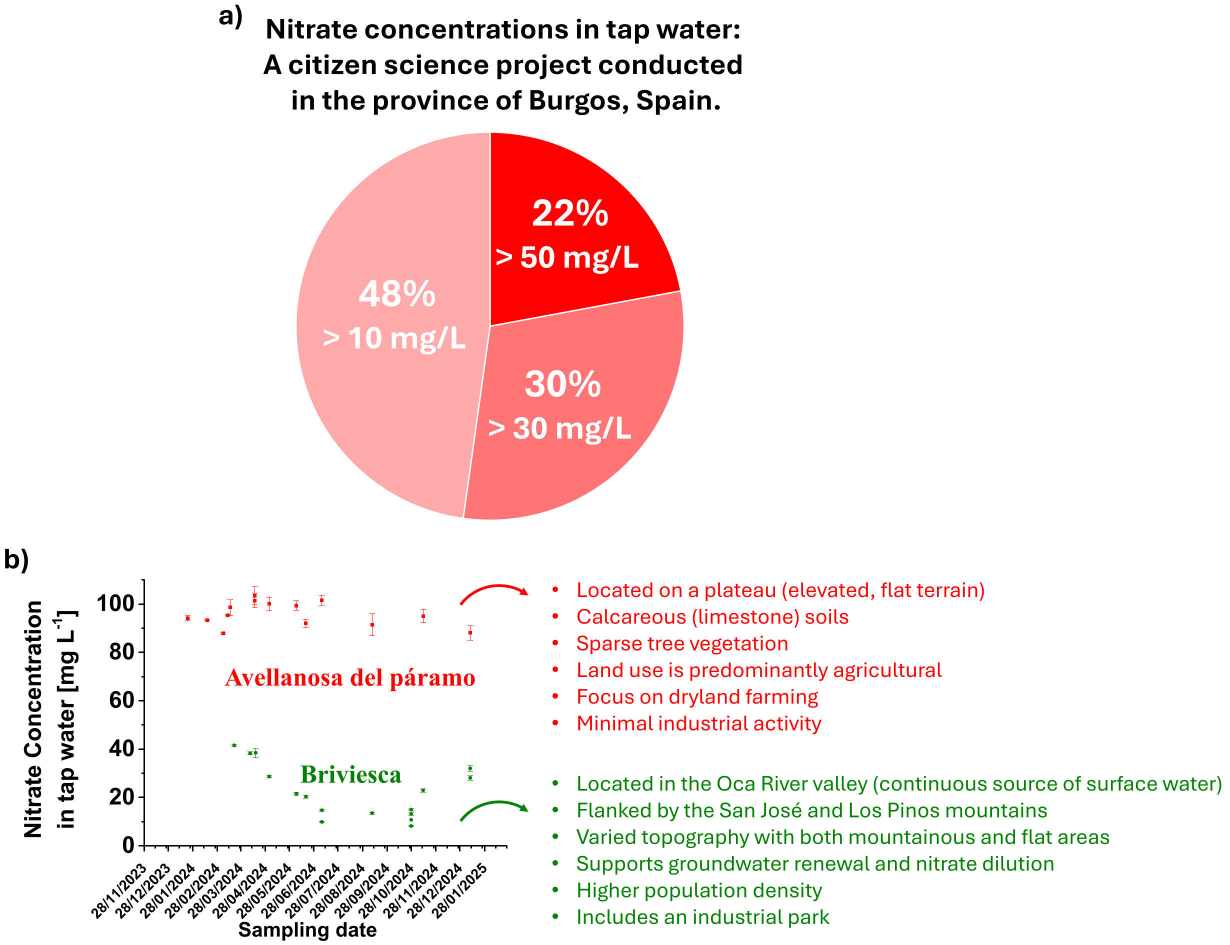

- Located on a plateau (elevated, flat terrain)
- Calcareous (limestone) soils
- Sparse tree vegetation
- Land use is predominantly agricultural
- Focus on dryland farming
- Minimal industrial activity

- Located in the Oca River valley (continuous source of surface water)
- Flanked by the San José and Los Pinos mountains
- Varied topography with both mountainous and flat areas
- Supports groundwater renewal and nitrate dilution
- Higher population density
- Includes an industrial park

Fig. 2. a) Graphical summary of the citizen science project conducted in the province of Burgos, Spain. b) Annual variation of nitrate concentrations in drinking water from Avellanosa del Páramo and Briviesca (Burgos, Spain).

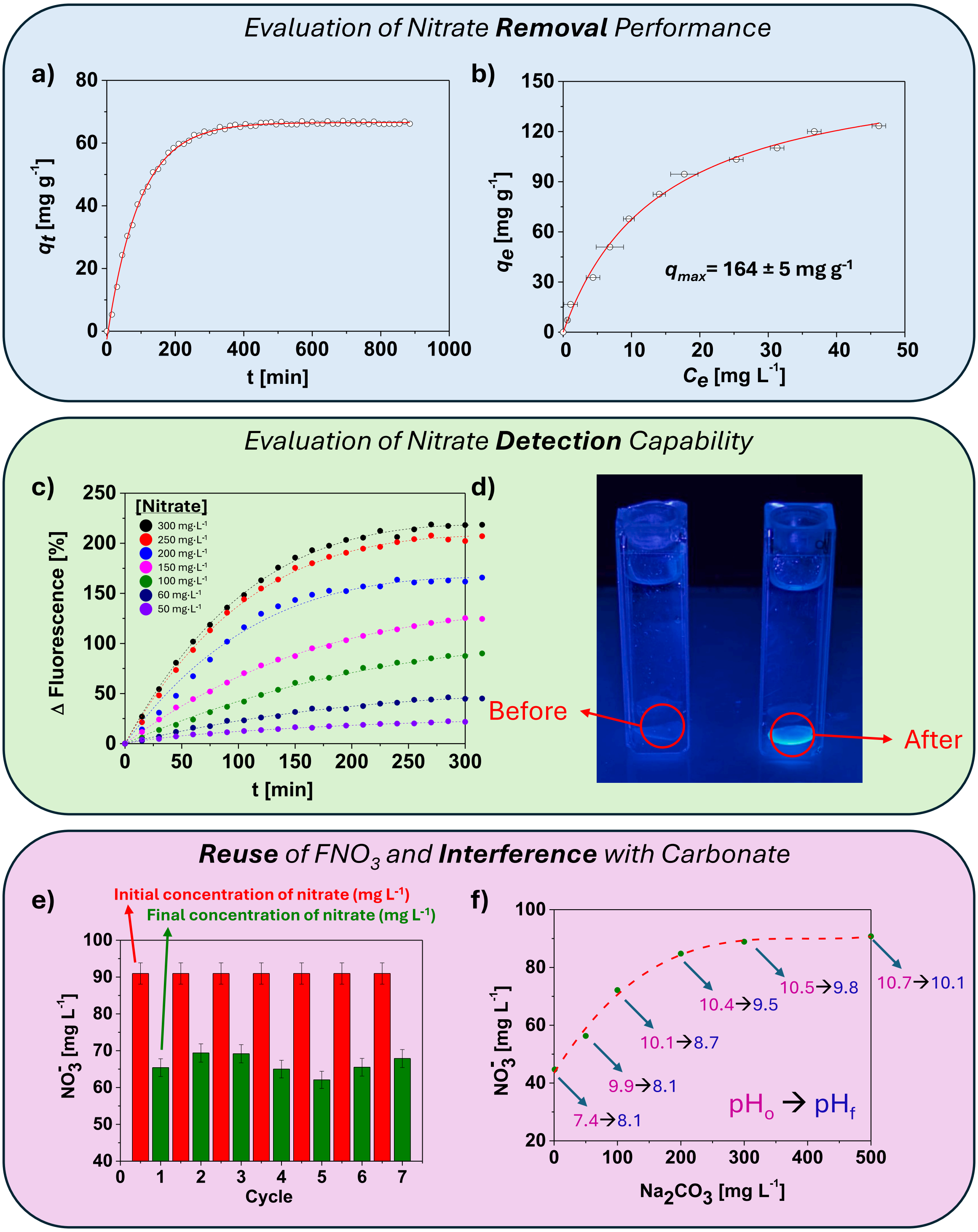

Fig. 3. a) Crank's dual-resistance model applied to adsorption kinetics at 40 ppm and 25 °C. b) Langmuir adsorption isotherm at 25 °C. c) Time-dependent increase in fluorescence intensity after exposure to nitrate solutions of varying concentrations. d) Visual change in fluorescence of FNO_3 before and after exposure to a 100 $mg\cdot L^{-1}$ nitrate solution. e) Reusability performance of FNO_3 over seven adsorption–regeneration cycles using real tap water. f) Interference study showing the effect of increasing carbonate concentrations on nitrate removal efficiency. The y-axis represents the nitrate concentration after treatment with FNO_3, starting from an initial nitrate concentration of 100 $mg\cdot L^{-1}$. Each data point also displays the initial and final pH of the solution before and after treatment with FNO_3, respectively.

3.2. One-year monitoring of nitrate concentrations

A common argument presented by certain administrative bodies is that nitrate levels in drinking water are subject to significant variability throughout the year. This variability is often attributed to two primary factors: (1) the application of fertilizers during sowing periods in the early months of the year, and (2) rainfall events that facilitate the leaching of nitrates into groundwater sources, potentially impacting water catchments.

In our study, we conducted a year-long monitoring of two locations within the province of Burgos, with samples collected by two of our researchers residing in these municipalities. The findings revealed two distinct patterns (Fig. 2b): (i) Avellanosa del Páramo: nitrate concentrations remained consistently high throughout the year, averaging approximately 100 mg·L^{-1}—twice the legal limit. This locality is situated on a plateau characterized by elevated, flat terrain with calcareous soils and sparse arboreal vegetation. The land use is predominantly agricultural, focusing on dryland farming with minimal industrial activity. The combination of intensive fertilizer use, limited groundwater renewal, and the absence of surface water bodies for dilution contributes to the area functioning as a persistent nitrate reservoir, indicating a chronic contamination issue that is challenging to remediate in the short term. (ii) Briviesca: in contrast, this locality exhibited seasonal variations in nitrate levels, with concentrations decreasing between April and September (post-rainy season) and increasing from October to March. Briviesca is located in the valley of the Oca River, flanked by the San José and Los Pinos mountains, featuring a more varied topography with both mountainous and flat regions. The Oca River provides a continuous source of surface water, enhancing groundwater renewal and facilitating nitrate dilution. Additionally, the area has a higher population density and includes an industrial park, factors that also influence nitrate levels, particularly during periods of reduced precipitation.

Results indicate that nitrate concentrations in drinking water are not solely dependent on seasonal factors but are significantly influenced by the hydrogeological characteristics and aquifer dynamics of each municipality.

3.3. Sorption study. Evaluation of nitrate removal performance

The adsorption process in solution consists of several sequential transport stages. First, the solute moves from the bulk solution toward a thin boundary layer surrounding FNO$_3$, a step known as external transport. Next, the solute diffuses through this boundary layer to reach FNO$_3$ś surface, a process referred to as external mass transfer. Subsequently, the solute diffuses within the FNO$_3$ particles, known as intraparticle diffusion. Finally, the solute is adsorbed onto the active sites of FNO$_3$. To analyse the adsorption kinetics in this study, two primary mathematical approaches were employed: the *Surface Reaction Model (SRM)* and the *Mass Transfer Reaction Model (MTM)*. The results of this preliminary analysis (more information in SM-Section S5), showed that the model that best fit the data was dual resistance (intraparticle and film diffusion). The results are showed in Fig. 3a.

The experimental values of q_e and C_e obtained (Fig. 3b) were fitted to the *Langmuir* adsorption isotherm, as described by Eq. (4).

$$q_e = \frac{q_{\max} K_L C_e}{1 + K_L C_e} \tag{4}$$

Langmuir was the first to propose a kinetic theory of adsorption on a flat surface (Langmuir, 1918). This model describes the adsorption of a monolayer on a homogeneous surface, with a fixed number of sites where adsorption of a single molecule occurs. In this equation, q_{max} (mg·g^{-1}) represents the maximum amount of adsorbate per unit weight of adsorbent required to form a complete monolayer on the surface, and K_L (L·mg^{-1}) is the affinity constant of the adsorbate for the adsorbent binding sites. These two constants enable the calculation of the thermodynamic equilibrium constant, K_c, as the product of both, according to Eq. (5):

$$K_c = K_L q_{\max} \tag{5}$$

From Eqs. (4) and (5), the following parameters were obtained: K_L= 0.070 ± 0.006 L·mg^{-1}, q_{max}= 164 ± 5 mg·g^{-1} , R^2= 0.9952,

Table 1

Estimated amount of FNO$_3$ (g) required to treat 1 L of water with varying initial and final nitrate concentrations, based on Langmuir model parameters. The vertical column in bold indicates the initial nitrate concentration (mg·L^{-1}) before using the FNO$_3$ film, and the horizontal row in bold indicates the final nitrate concentration (mg·L^{-1}) after treatment.

		Desired nitrate concentration (mg·L^{-1}) after treatment with FNO$_3$														
		50			**40**			**30**			**20**			**10**		
Nitrate concentration (mg·L^{-1}) before treatment with FNO$_3$	**150**	0.80	±	0.10	0.90	±	0.20	1.10	±	0.20	1.40	±	0.20	2.10	±	0.30
	140	0.70	±	0.10	0.80	±	0.10	1.00	±	0.20	1.30	±	0.20	1.90	±	0.30
	130	0.60	±	0.10	0.70	±	0.10	0.90	±	0.20	1.20	±	0.20	1.80	±	0.30
	120	0.55	±	0.10	0.70	±	0.10	0.80	±	0.10	1.00	±	0.20	1.60	±	0.20
	110	0.47	±	0.09	0.60	±	0.10	0.70	±	0.10	0.90	±	0.20	1.50	±	0.20
	100	0.39	±	0.07	0.50	±	0.09	0.60	±	0.10	0.80	±	0.10	1.30	±	0.20
	90	0.31	±	0.06	0.41	±	0.07	0.54	±	0.09	0.70	±	0.10	1.20	±	0.20
	80	0.24	±	0.04	0.33	±	0.06	0.45	±	0.08	0.63	±	0.10	1.00	±	0.20
	70	0.16	±	0.03	0.25	±	0.04	0.36	±	0.06	0.52	±	0.09	0.90	±	0.10
	60	0.08	±	0.01	0.17	±	0.03	0.27	±	0.05	0.42	±	0.07	0.74	±	0.11
	50	-	-	-	0.08	±	0.01	0.18	±	0.03	0.31	±	0.05	0.59	±	0.09

K_C= 710 ± 80. It is worth noting that we calculated the q_{max} for a nitrate exchange commercial resin (Dupla, Duresin N 80563), obtaining a value of approximately 45 mg·g^{-1} , therefore, our material exhibits a nitrate adsorption capacity that is 3.6 times higher than that of the commercial counterpart ("Dupla, 2025").

Using these values, it is possible to calculate the amount of adsorbent required to remove a specific quantity of adsorbate from a solution containing only nitrates, as shown in Table 1. This table is of high relevance, as it provides end users with guidance on the required amount of FNO_3 to use, based on the initial nitrate concentration in their local water supply and the desired final nitrate concentration after treatment with FNO_3.

3.4. Fluorescence study. Evaluation of nitrate detection capability

In addition to removing nitrates from the medium, FNO_3 also undergoes a fluorescence turn-on (OFF–ON) process as the concentration of adsorbed species increases. This phenomenon is primarily attributed to the presence of chloride ions within FNO_3, which quench the fluorescence of the coumarin motifs. Upon displacement of the chlorides by nitrates, the fluorescence is restored. This behaviour not only enables the detection of nitrates in the medium but also allows their quantification.

Fig. 3c illustrates the progressive increase in the fluorescence intensity of the material over time following its immersion in solutions with varying nitrate concentrations, ranging from 50 ppm to 300 ppm. A direct correlation is observed between the nitrate concentration in the solution and the emitted fluorescence intensity, confirming the ability of FNO_3 to respond sensitively and rapidly to changes in the concentration of this anion.

From a more qualitative perspective, Fig. 3d displays images of the material before and after immersion in a nitrate solution at a concentration of 100 mg·L^{-1}. These images demonstrate that the material enables straightforward and clear visual detection, facilitating its use by non-specialized users. This feature is particularly relevant for citizen science applications, where accessibility and ease of use are critical for participatory water quality monitoring.

Although the calculated limits of detection (*LOD*, 4.26 mg·L^{-1}), and quantification (*LOQ*, 12.92 mg·L^{-1}) are not exceptionally low—particularly when compared to commercial systems such as those developed by Hanna Instruments, which can achieve detection levels as low as 0.01 mg·L^{-1} of NO_3-N—they are nonetheless adequate for the intended application ("Espectrofotómetro portátil DR1900 | Hach España-Aspectos Generales | Hach," 2025). This is because they remain more than an order of magnitude below the maximum concentration limits established by both European and Spanish water quality regulations (European Parliament and the Council of the European Union, 2020; Ministry of the Presidency, 2023). It is important to note that many of the most sensitive commercial systems rely on indirect detection methods involving the formation of azo dyes and absorbance measurements within the 340–800 nm range, which require derivatization steps. In contrast, our method allows direct nitrate detection based on fluorescence without the need for chemical derivatization, with the added advantage that the material cost is relatively low, approximately €1.7 per gram. For nitrate concentrations around several milligrams per litre, the response time of the material ranges between 50 and 100 min, depending on the presence of potential interfering species. Furthermore, unlike commercial solutions that necessitate the purchase of specialized instrumentation and consumable reagents, our system operates without the need for either equipment or reagents, offering a simpler, more cost-effective, and user-friendly alternative for decentralized and participatory water monitoring.

3.5. Reusability of FNO_3, carbonate interference, and pH influence

3.5.1. Reusability of FNO_3

One of the key requirements for FNO_3 is its reusability, ideally allowing the regeneration process to be performed at home using readily available household reagents, such as common table salt. In our case, we employed tap water from Avellanosa del Páramo (Spain) to test it. Our citizen science study demonstrated that the nitrate concentration in the local tap water was approximately 100 mg·L^{-1}. As a proof of concept, a volume of 3.5 mL of solution with an initial nitrate concentration of approximately 100 mg·L^{-1} was contacted with 1.6 mg of FNO_3. After 2 h, the nitrate concentration decreased to 67 mg·L^{-1}, demonstrating effective adsorption. The material was then regenerated by immersion in a 500 mg·L^{-1} potassium chloride solution for 120 min and reused the following day in fresh Avellanosa del Páramo water with the same nitrate levels. This adsorption-regeneration cycle was repeated daily for a full week. As shown in Fig. 3e, FNO_3 maintained its adsorption efficiency consistently across all seven cycles, confirming its stability and effective reusability under practical, user-friendly conditions.

However, this reuse study revealed a critical aspect that needed to be addressed: according to the adsorption equilibrium data presented in Table 1, the residual nitrate concentration in the water treated with FNO_3 should theoretically be approximately 47 mg·L^{-1}, rather than the initially observed 67 mg·L^{-1}. This discrepancy prompted the hypothesis that the nitrate removal efficiency of FNO_3 could be affected by the presence of competing anions in the water, particularly carbonates and bicarbonates. These anions are commonly found in groundwater from calcareous regions and are known to interfere with anion exchange processes.

This observation also highlights that the potential use of this material by end users would necessarily need to be accompanied by an initial assessment of the water intended for purification. Such an assessment would allow the definition of critical operating parameters, including the immersion time required to reach a safe nitrate concentration, the number of uses possible before regeneration, and the number of regeneration cycles feasible before disposal. Importantly, all these parameters will strongly depend on the specific characteristics of each individual water source.

3.5.2. Interference and pH study

In this regard, a chemical analysis conducted by the company DXD Soluciones Químicas S.L. indicated that the water from the municipality of Avellanosa del Páramo exhibited a total alkalinity of 180 mg·L^{-1}, suggesting a significant presence of carbonate and bicarbonate species. Given that these anions are common constituents of groundwater in regions with limestone geology—and are routinely included in standard water quality analyses—it was deemed appropriate to conduct a brief interference study to evaluate their impact on the nitrate removal performance of FNO$_3$.

For this purpose, a series of sodium carbonate solutions were prepared at varying concentrations, ranging from 0 to 500 mg·L^{-1}, all containing a fixed nitrate concentration of 95 mg·L^{-1}. The experiments were conducted in Milli-Q water to eliminate background ionic interference. As shown in Fig. 3 f, an increase in carbonate concentration resulted in a progressively higher residual concentration of nitrates in the solution after treatment with FNO$_3$. This trend clearly indicates that carbonate and/or bicarbonate ions act as significant interferents, competing with nitrates for the active adsorption sites in FNO$_3$ and thereby reducing its overall removal efficiency.

To better understand the role of carbonate interference in nitrate adsorption, it was necessary to consider the solution pH, as the carbonate/bicarbonate pair functions as a buffering system. Depending on the pH, the dominant species will be either carbonate (CO_3^{2-}) or bicarbonate (HCO_3^-). Therefore, both the initial and final pH values were measured in all sodium carbonate solutions used in the interference experiment, as shown in Fig. 3f.

Carbonate originates from a weak acid, thus acting as a strong base that reacts with water to produce bicarbonate and hydroxide ions (OH^-). In turn, bicarbonate also reacts with water to generate carbonic acid and additional hydroxide ions, according to the following equilibrium, defined by Eq. (6):

$$\begin{aligned} &CO_3^{2-} + H_2O \rightleftarrows HCO_3^- + OH^- \\ &HCO_3^- + H_2O \rightleftarrows H_2CO_3 + OH^- \end{aligned} \tag{6}$$

In this system, pH is crucial as it determines the concentration of each species at equilibrium. At the point with the lowest carbonate concentration (Fig. 3f), the initial pH was 7.4 and increased to 8.1 after treatment with FNO$_3$. Since adsorption is diffusion-controlled, higher concentrations correspond to a faster adsorption rate. At approximately pH 8, the dominant species is bicarbonate (>98 %), which competes with nitrate for active sites, shifting the equilibrium toward increased formation of OH^-.

Interestingly, at higher carbonate concentrations, a slight decrease in the final pH is observed. This is because the carbonate, present in greater proportion, is also adsorbed alongside nitrate, shifting the equilibrium toward carbonate formation and thereby reducing the concentration of OH^-, which decreases the solution's basicity.

These observations also help explain the behaviour observed in the reuse assay with tap water from Avellanosa del Páramo, which had a pH of 7.8. Under these conditions, bicarbonate was the clearly predominant species (>98 %). This water exhibited an alkalinity of 180 mg·L^{-1} (expressed as $CaCO_3$), nearly twice the nitrate concentration. However, nitrate removal efficiency decreased by approximately 40 %, indicating a higher selectivity of the FNO$_3$ material toward nitrates compared to bicarbonate. On the other hand, comparing the affinity for nitrate and carbonate is not pertinent in this case, as at pH < 8.5 the presence of carbonate anions in drinking water is practically negligible.

To further investigate the pH dependence of nitrate adsorption by FNO$_3$, a series of controlled experiments were conducted with OH^- anions. A stock solution of nitrates (92 mg·L^{-1}) in distilled water with an initial pH of 6.24 was divided into five aliquots. Each aliquot was adjusted to a different initial pH by adding small volumes of NaOH, ensuring minimal dilution and maintaining consistent nitrate concentration across samples. Subsequently, 3.5 mL of each solution was treated with 1.63 mg of FNO$_3$, and UV-Vis absorbance measurements were recorded at time zero and after 500 min. Final pH values were also monitored. To understand the intrinsic effect of FNO$_3$ on solution pH, the material was immersed in nitrate-free distilled water. The pH of this blank solution increased from 6.5 to 7.35, suggesting the release or uptake of species affecting proton concentration.

As shown in Fig. 4, nitrate adsorption remained consistent across all tested pH values, indicating a broad operational range and

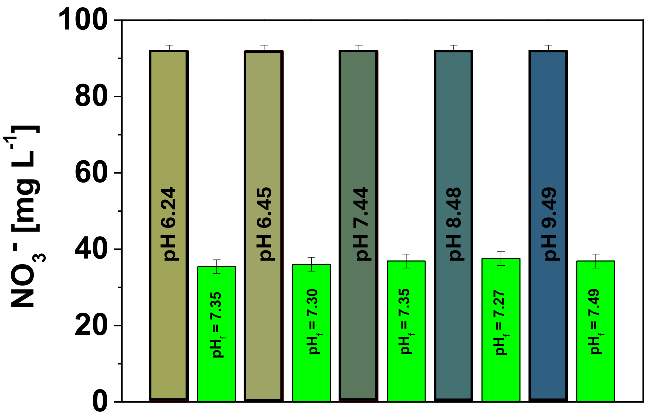

Fig. 4. Influence of initial pH on the nitrate adsorption efficiency of the FNO$_3$ material. Solutions containing 92 mg·L^{-1} of nitrates were adjusted to different pH values using NaOH and treated with 1.63 mg of material in 3.5 mL of solution. The bars show initial and final pH values and the amount of nitrate adsorbed after 500 min (light green). Results indicate that adsorption efficiency remains stable across the tested pH range, while the material exhibits a buffering effect that stabilizes the final pH around 7.35.

robustness of the material's performance under varying acid-base conditions. Interestingly, in the most alkaline solution, a final pH of 7.49 was observed, slightly above the standard post-treatment value of 7.35. This behaviour suggests partial adsorption of OH^- ions in basic conditions, without significant impact on nitrate removal. Conversely, in more acidic media (first two solutions), where $[H^+] > [OH^-]$, the carbonyl groups within FNO_3 acted as proton acceptors, buffering the system and leading to a rise in final pH. This buffering capacity mimics that of a weak base and highlights the material's stabilizing effect on solution pH—particularly relevant for real-world water treatment scenarios where incoming pH conditions may vary. In future studies, the potential of this type of material as a solid-phase pH buffering system (solid buffer) will be explored, given its ability to stabilize pH in solution.

3.6. LCA

The environmental analysis of the nitrate removal film reveals a distinct distribution of impacts across its life cycle stages.

Production phase. The primary contributors to environmental impact are the production of glass (used as a structural material), transport of inputs, electricity consumption, and specific functional monomers (NNZA, VP, SA-1025) along with additives such as the photoinitiator DMPA and the crosslinker EGDMA. The impact of glass mainly arises from the extraction and processing of metallic and mineral resources, while transport and electricity impacts are largely due to fossil fuel use in energy generation and logistics. The functional monomers and additives significantly contribute to categories such as ecotoxicity, human toxicity, and resource use; however, their inclusion is justified by the functional value they provide to nitrate capture. The final FNO_3 film product itself accounts for a very small fraction of the total impact, highlighting the system's functional efficiency (Fig. 5a).

Impact weighting and improvement opportunities. Normalization results indicate that fossil resource depletion and non-carcinogenic human toxicity are priority areas for improvement, with carcinogenic human toxicity primarily linked to N-vinyl-pyrrolidone and NNZA (Fig. 5b). Impact weighting based on the EF method identifies climate change and resource use as critical categories, largely due to material inputs and energy demands. Potential improvement strategies include substituting glass with bio-based or recycled materials, localizing supply chains, optimizing logistics, transitioning to renewable energy sources, and exploring more sustainable sourcing or reformulation of the monomers (Figs. 5c and 5d). These findings should be interpreted considering the innovative nature of the system and its current laboratory-scale implementation, which has yet to benefit from industrial optimization.

Use phase. The use phase of the film exhibits a favourable environmental profile. Treated effluent can be valorized as an agricultural input, partially substituting conventional nitrogen fertilizers, which generates net benefits across aquatic ecotoxicity, human toxicity, eutrophication, and resource use categories. The potential for reusing the water or the film as a fertilizer will be addressed in future studies. The damage assessment confirms these positive trends, especially in resource use, human health, and ecosystem-related categories. While per-cubic-meter benefits may appear moderate on a per capita basis, their relevance increases in localized or decentralized contexts where closing water and nutrient loops is prioritized (Fig. 5e and f).

Comparison with conventional technologies. Compared to nitrification-denitrification or anammox processes (Vineyard et al., 2021), the film provides a more compact and versatile approach, with relatively lower impacts in some categories and higher in others, mainly due to specialized components. Compared to reverse osmosis or Ecogranularwater (Alguacil-Duarte et al., 2022), the film exhibits higher impacts per functional unit, attributable to its low TRL, laboratory-scale implementation, and lack of process optimization or input recovery.

3.7. Toxicology study. Determination of HepG2 cells response to the different water samples

Given that the primary route of exposure to drinking water is oral ingestion, a hepatic cell line was selected as the *in vitro* model, as the liver is the main organ responsible for the metabolism of ingested compounds and therefore represents a biologically relevant system for toxicity assessment. The viability of the human hepatocarcinoma cell line HepG2 after 24 h of exposure to the highest tested concentration of water was evaluated using the *MTT assay*. This colorimetric test measures cellular metabolic activity based on the reduction of MTT to a purple formazan product by metabolically active cells, with absorbance measured at 590 nm. As shown in Fig. 6, no substantial reduction in cell viability was observed in the water samples compared to the negative control. The *MTT assay* results indicate that 24-hour exposure of FNO_3 to the water samples did not induce cytotoxic effects.

4. Practical applications and future research prospects

The multifunctional FNO_3 polymeric thin films developed in this work have clear practical applications in both water treatment and environmental monitoring. Their high selectivity and reusability make them suitable for decentralized nitrate removal in small-scale or rural water systems, where conventional technologies such as reverse osmosis or ion-exchange resins are inefficient, wasteful, or cost-prohibitive. The integrated fluorescence signal provides a simple visual cue for saturation, enabling non-specialized personnel and community members to monitor water quality effectively. This combination of curative and sensory functionality supports citizen science initiatives, allowing local communities to participate in environmental monitoring and fostering awareness of nitrate pollution and preventive actions.

Future research should focus on several aspects to enhance the material's applicability and performance. First, detection accuracy and precision under a wider range of environmental conditions should be assessed. Second, interference studies should be expanded to include diverse ions and complex water matrices commonly found in natural and agricultural settings. Third, scaling up production while maintaining material quality and cost-effectiveness will be essential for practical deployment. Additionally, long-term stability, repeated reuse, and integration with circular recovery strategies for captured nitrates should be investigated. Finally, further LCA and

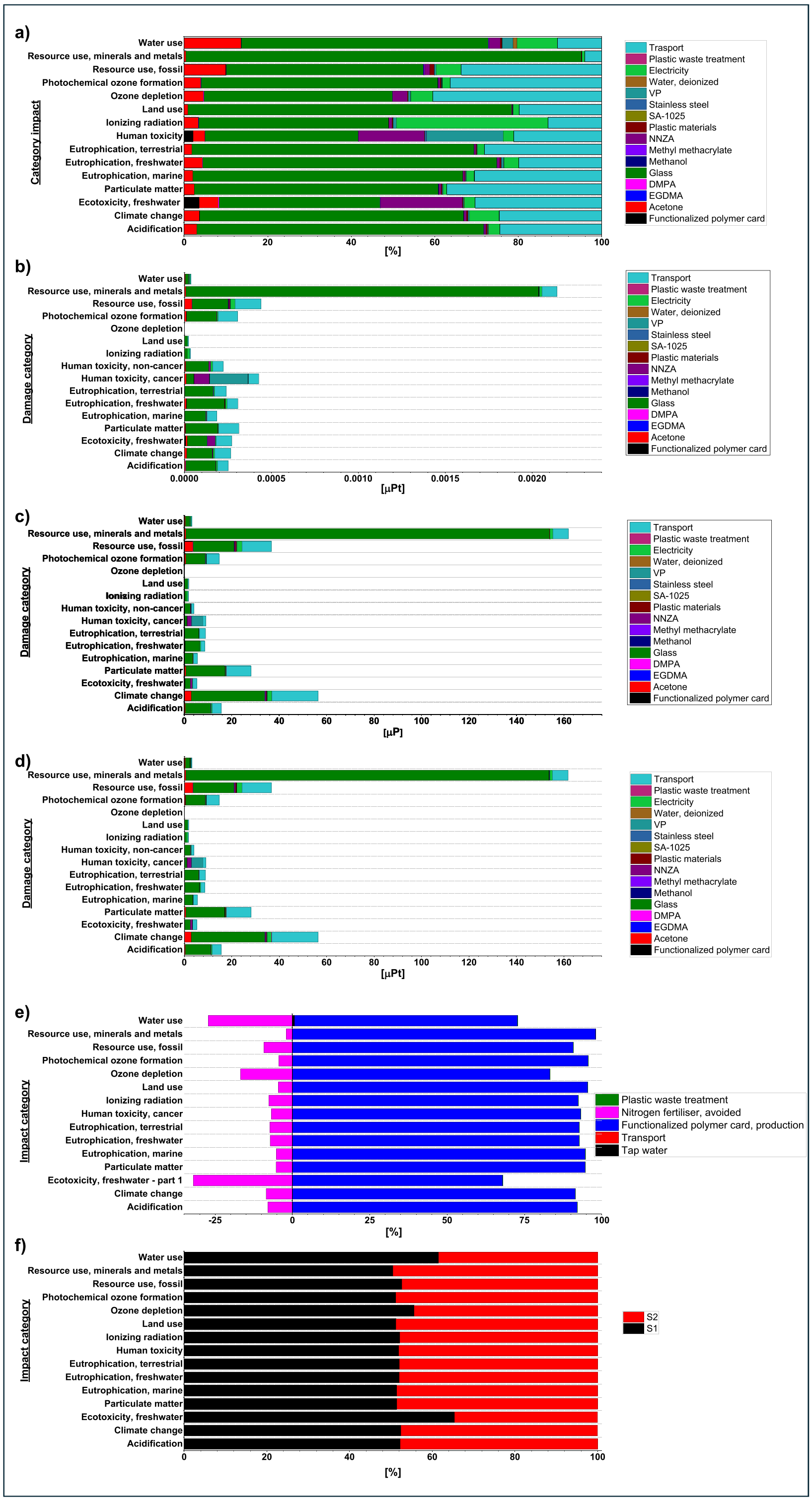

(caption on next page)

Fig. 5. a) Percentage contribution of different processes and materials to the environmental impact by category (characterization) during the production phase of the functional film for nitrate removal. b) Normalized environmental impact by category associated with the production of the functional film for nitrate removal. This diagram provides a relative comparison among impact categories according to the Environmental Footprint 3.1 method. c) Weighted environmental impact by category for the production of the functional film for nitrate removal, based on the Environmental Footprint 3.1 method. d) Contribution of each process to the total environmental impact (aggregated single score) during the production of the functional film for nitrate removal, as assessed using the Environmental Footprint 3.1 method. e) Characterization of the environmental impact by category of the processes involved during the use phase of the functional film for nitrate removal, according to the Environmental Footprint 3.1 method. f) Comparison of the environmental footprint profile between two use scenarios of the film: S1 (without valorization of the regenerated water) and S2 (with valorization as fertilizer), expressed as the percentage of net impact per category.

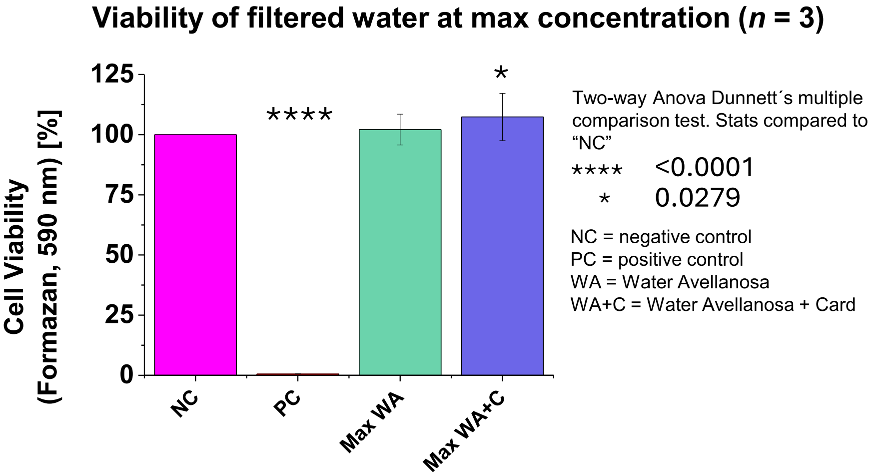

Fig. 6. a) Viability of HepG2 cells treated with different water samples at their maximum concentration. Results are expressed as a percentage of negative control (untreated cells). Data represent the *mean (± standard deviation, SD)* of 3 biological replicates with 4 technical replicates. Differences are established using a *Two-way ANOVA* followed by a multicomparison test (*Dunnett's test*), and considered significant when $P \leq 0.05$.

toxicological evaluations will help ensure environmental safety and support industrial-scale implementation.

5. Conclusions

This work presents a comprehensive approach to nitrate pollution by integrating multifunctional polymeric thin films (FNO_3) with citizen science initiatives. FNO_3 combines nitrate removal and visual detection via fluorescence, demonstrating high selectivity, reusability, and practical limits of detection for real-world applications. Citizen participation revealed strong engagement, highlighting public demand for information and preventive action. Field studies showed site-specific nitrate variations, emphasizing the need for tailored interventions. Preliminary LCA and toxicological evaluations confirmed the material's environmental safety and scalability. Overall, this approach provides a low-cost, decentralized, and circular solution to nitrate pollution, empowering communities, promoting awareness, and supporting environmental and economic resilience. Future work should refine detection accuracy, expand interference studies, and optimize industrial-scale production, advancing FNO_3 toward practical deployment in water treatment.

CRediT authorship contribution statement

Laura Gómez-Cuadrado: Writing – review & editing, Writing – original draft, Methodology, Investigation. **Sonia Martel:** Writing – review & editing, Writing – original draft, Formal analysis. **Rocío BARROS:** Writing – review & editing, Methodology, Funding acquisition, Conceptualization. **Vallejos Saul:** Writing – review & editing, Writing – original draft, Supervision, Project administration, Methodology, Investigation, Funding acquisition, Conceptualization. **Vallejo-García Jorge:** Writing – original draft, Validation, Methodology, Investigation, Conceptualization. **Raquel Hernández-Ruiz:** Writing – review & editing, Writing – original draft, Funding acquisition. **Alba Torija-López:** Validation, Methodology, Investigation, Formal analysis. **Miriam Trigo-López:** Writing – review & editing, Writing – original draft, Methodology. **Saturnino Ibeas:** Writing – original draft, Validation, Methodology, Investigation, Formal analysis.

Declaration of Competing Interest

The authors declare that they have no known competing financial interests or personal relationships that could have appeared to influence the work reported in this paper.

Acknowledgements

We gratefully acknowledge the financial support provided by all funders. Author S. Vallejos received Grant PID2023–147301OB-I00 and Grant 8138165958–165958–57–425 funded by MICIU/AEI /10.13039/501100011033 and FEDER, EU. The financial support provided by Fondo Europeo de Desarrollo Regional-European Regional Development Fund (FEDER, ERDF) and Regional Government of Castilla y León -Consejería de Educación, Junta de Castilla y León- (BU025P23) is gratefully acknowledged. This work was supported by the Regional Government of Castilla y León (Junta de Castilla y León) and by the Ministry of Science and Innovation MICIN and the European Union *NextGenerationEU* PRTR. This project has received funding from the LIFE Programme of the European Union under Grant Agreement N° 101215633 - LIFE NITRAZENS. J. L. Vallejo-García received the grant PRE2021–09812 funded by MCIN/AEI/ 10.13039/501100011033 and by "ESF Investing in your future". Author Saul Vallejos received grant BG22/00086 funded by Spanish Ministerio de Universidades.

Appendix A. Supporting information

Supplementary data associated with this article can be found in the online version at doi:10.1016/j.eti.2025.104595.

Data availability

No data was used for the research described in the article.

References

Alguacil-Duarte, F., González-Gómez, F., Romero-Gámez, M., 2022. Biological nitrate removal from a drinking water supply with an aerobic granular sludge technology: an environmental and economic assessment. J. Clean. Prod. 367, 133059. https://doi.org/10.1016/j.jclepro.2022.133059.

Arnaiz, A., Guembe-García, M., Martínez, M., Trigo-López, M., González, E., Otsuka, I., Vallejos, S., 2025. Naked-eye detection of *Legionella pneumophila* using smart fluorogenic polymers prepared as hydrophilic films, coatings, and electrospun nanofibers. Sens. Actuators B Chem. 425, 136976. https://doi.org/10.1016/j.snb.2024.136976.

Arnaiz, A., Guirado-Moreno, J.C., Guembe-García, M., Barros, R., Tamayo-Ramos, J.A., Fernández-Pampín, N., García, J.M., Vallejos, S., 2023. Lab-on-a-chip for the easy and visual detection of SARS-CoV-2 in saliva based on sensory polymers. Sens. Actuators B Chem. 379, 133165. https://doi.org/10.1016/j.snb.2022.133165.

Badea, M., Amine, A., Palleschi, G., Moscone, D., Volpe, G., Curulli, A., 2001. New electrochemical sensors for detection of nitrites and nitrates. J. Electroanal. Chem. 509, 66–72. https://doi.org/10.1016/S0022-0728(01)00358-8.

Bustamante, S.E., Vallejos, S., Pascual-Portal, B.S., Muñoz, A., Mendia, A., Rivas, B.L., García, F.C., García, J.M., 2019. Polymer films containing chemically anchored diazonium salts with long-term stability as colorimetric sensors. J. Hazard. Mater. 365, 725–732. https://doi.org/10.1016/j.jhazmat.2018.11.066.

Donat-Vargas, C., Kogevinas, M., Castaño-Vinyals, G., Pérez-Gómez, B., Llorca, J., Vanaclocha-Espí, M., Fernandez-Tardon, G., Costas, L., Aragonés, N., Gómez-Acebo, I., Moreno, V., Pollan, M., Villanueva, C.M., 2023. Long-term exposure to nitrate and trihalomethanes in drinking water and prostate cancer: a multicase–control study in Spain (MCC-Spain). Environ. Health Perspect. 131. https://doi.org/10.1289/EHP11391.

Dupla, n.d. Duresin N. ⟨https://dupla.com/ES/80563/duresin-n⟩- (Accessed 19 August 2025).

Espectrofotómetro portátil DR1900 | Hach España - Aspectos Generales | Hach, 2025. ⟨https://es.hach.com/espectrofotometros/espectrofotometro-portatil-dr1900/family?productCategoryId=25116633784⟩ (Accessed 16 July 2025).

European Parliament and the Council of the European Union, 2020. Directive (EU) 2020/2184 of the Council of 16 December 2020 on the quality of water intended for human consumption (recast). Off. J. Eur. Union L 435, 1–62.

Gaona-Ruiz, M., Vallejo-García, J.L., Arnaiz, A., Sedano-Labrador, C., Trigo-López, M., Rodríguez, A., Carrillo, C., Vallejos, S., 2024. Smart polymers and smartphones for betalain measurement in cooked beetroots. Food Chem. 459, 140358. https://doi.org/10.1016/j.foodchem.2024.140358.

García Pérez, J.M., García García, F.C., Vallejos, S., Trigo, M., Reglero-Ruiz, J.A., 2022. Smart Polymers. Principles and Applications. De Gruyter, Boston. https://doi.org/10.1515/9781501522468.

García Pérez, J.M., Vallejos, S., Trigo-López, M., 2024. Sensory Polymers: From their Design to Practical Applications. Elsevier, Amsterdam.

Guembe-García, M., Utzeri, G., Valente, A.J.M., Ibeas, S., Trigo-López, M., García, J.M., Vallejos, S., 2024. Efficient extraction of textile dyes using reusable acrylic-based smart polymers. J. Hazard. Mater. 476, 135006. https://doi.org/10.1016/j.jhazmat.2024.135006.

Hutchins, R.S., Bachas, L.G., 1995. Nitrate-selective electrode developed by electrochemically mediated imprinting/doping of polypyrrole. Anal. Chem. 67, 1654–1660. https://doi.org/10.1021/ac00106a002.

Jacobsen, B.H., Hansen, B., Schullehner, J., 2024. Health-economic valuation of lowering nitrate standards in drinking water related to colorectal cancer in Denmark. Sci. Total Environ. 906, 167368. https://doi.org/10.1016/j.scitotenv.2023.167368.

Jobgen, W.S., Jobgen, S.C., Li, H., Meininger, C.J., Wu, G., 2007. Analysis of nitrite and nitrate in biological samples using high-performance liquid chromatography. J. Chromatogr. B 851, 71–82. https://doi.org/10.1016/j.jchromb.2006.07.018.

Langmuir, I., 1918. The adsorption of gases on plane surfaces of glass, mica and platinum. J. Am. Chem. Soc. 40, 1361–1403. https://doi.org/10.1021/ja02242a004.

Lin, J., Wang, M., Ang, S., Zhu, J., 2007. Development of a polypyrrole modified gold microelectrode for soil nitrate detection. International Conference on Mechatronics and Automation. IEEE, pp. 3396–3400. https://doi.org/10.1109/ICMA.2007.4304108.

Majumdar, D., 2003. The blue baby syndrome. Resonance 8, 20–30. https://doi.org/10.1007/BF02840703.

Mediaset, 2025a. Casi 54,000 personas beben agua contaminada en Burgos: ¿cuáles son las causas? *Mediaset*. ⟨https://www.telecinco.es/noticias/sociedad/20240426/agua-burgos-no-apta-consumo-nivel-nitratos-universidad_18_012334071.html⟩ (accessed 5 July 2025).

Mediaset, 2025b. El agua de 39 localidades de Burgos no es apta para su consumo por sus altos niveles de nitratos, según un estudio. *Mediaset*. ⟨https://www.telecinco.es/noticias/sociedad/20240426/agua-burgos-no-apta-consumo-nivel-nitratos-universidad_18_012334071.html⟩ (accessed 5 July 2025).

Ministry of the Presidency, 2023. Real Decreto 3/2023, de 10 de enero, por el que se establecen los criterios técnico-sanitarios de la calidad del agua de consumo, su control y suministro. Boletín Of. Estado, 9.

Miranda, K.M., Espey, M.G., Wink, D.A., 2001. A rapid, simple spectrophotometric method for simultaneous detection of nitrate and nitrite. Nitric Oxide 5, 62–71. https://doi.org/10.1006/niox.2000.0319.

Mosmann, T., 1983. Rapid colorimetric assay for cellular growth and survival: Application to proliferation and cytotoxicity assays. J. Immunol. Methods 65, 55–63. https://doi.org/10.1016/0022-1759(83)90303-4.

Nitrate Test Strips, colorimetric 10–500 mg L-1 (NO3-), MQuant®, for use with MQuant® StripScan App | Sigma-Aldrich, 2025. ⟨https://www.sigmaaldrich.com/ES/es/product/mm/110020⟩ (Accessed 5 July 2025).

Spain. Head of State, 1985. Ley 7/1985, de 2 de abril, Reguladora de las Bases del Régimen Local. Boletín Of. Estado vol. 80.

Vallejo-García, J.L., Arnaiz, A., Busto, M.D., García, J.M., Vallejos, S., 2023. Film-shaped reusable smart polymer to produce lactose-free milk by simple immersion. Eur. Polym. J. 200, 112495. https://doi.org/10.1016/j.eurpolymj.2023.112495.

Vallejos, S., Hernando, E., Trigo, M., García, F.C., García-Valverde, M., Iturbe, D., Cabero, M.J., Quesada, R., García, J.M., 2018. Polymeric chemosensor for the detection and quantification of chloride in human sweat. Application to the diagnosis of cystic fibrosis. J. Mater. Chem. B 6, 3735–3741. https://doi.org/10.1039/c8tb00682b.

Vineyard, D., Hicks, A., Karthikeyan, K.G., Davidson, C., Barak, P., 2021. Life cycle assessment of electrodialysis for sidestream nitrogen recovery in municipal wastewater treatment. Clean. Environ. Syst. 2, 100026. https://doi.org/10.1016/j.cesys.2021.100026.

Ward, M.H., Jones, R.R., Brender, J.D., de Kok, T.M., Weyer, P.J., Nolan, B.T., Villanueva, C.M., van Breda, S.G., 2018. Drinking water nitrate and human health: an updated review. Int. J. Environ. Res. Public Health 15, 1557. https://doi.org/10.3390/ijerph15071557.

Water and Sanitation-United Nations Sustainable Development, n.d. ⟨https://www.un.org/sustainabledevelopment/water-and-sanitation/⟩ (Accessed 5 July 2025).

Supplementary material (SM)

Multifunctional Smart Polymers and Citizen Science for a Comprehensive Approach to Nitrate Pollution: Curative and Preventive Strategies

J. Lucas VALLEJO-GARCÍA[a], Raquel HERNÁNDEZ-RUIZ[a], Alba TORIJA-LÓPEZ[a], Miriam TRIGO-LÓPEZ[a], Saturnino IBEAS[a], Laura GÓMEZ-CUADRADO[b], Sonia MARTEL[b], Rocío BARROS[b], Saúl VALLEJOS[a,*]

[a] Grupo de Polímeros. Departamento de Química, Facultad de Ciencias, Universidad de Burgos, Plaza de Misael Bañuelos s/n, 09001 Burgos, Spain.

[b] International Research Center in Critical Raw Materials for Advanced Industrial Technologies (ICCRAM), R&D Center, Universidad de Burgos, Plaza de Misael, Bañuelos s/n, 09001 Burgos, Spain.

*Corresponding author: Dr Vallejos (svallejos@ubu.es)

Table of contents

S1. RESULTS OF THE CITIZEN SCIENCE PROJECT

Table S1. Citizen Science Project Results: Nitrate Concentration in Tap Water Samples

TAP WATER SAMPLES (SUMMARY)				
	Nº of samples	**%**		
TOTAL	247	100		
> 50 mg L^{-1}	55	22		
> 30 mg L^{-1}	75	30		
> 10 mg L^{-1}	119	48		

*In most towns, the municipal water is only treated with chlorination. Only towns with more than 1,000 inhabitants operate proper drinking water treatment plants, with standard procedures including coagulation, ozonation, chlorination, and filtration.
*Samples were analyzed 1–7 days after collection and stored under refrigeration until analysis.

TAP WATER							
Town	**Source**	**Nitrate Concentration (mg L^{-1})**	**Standard Error**	**Date of Analysis**	**Coordinates**	**Area (km^2)**	**Population**
Villatuelda	Tap Water	134.35	3.00	05/04/2024	41°48'54"N 3°52'55"W	15.3	53
Guadilla de Villamar	Tap Water	115.79	3.94	21/03/2024	42°31'31"N 4°10'28"W	23.76	93
Solduengo de Bureba	Tap Water	112.96	3.00	06/03/2024	42°39'41"N 3°20'32"W	12	16
Quintanilla de Riofresno	Tap Water	103.46	2.80	22/03/2024	42°32'24"N 4°12'29"W	1.36	24
Citores del Páramo	Tap Water	103.35	1.37	20/03/2024	42°23'41"N 3°58'58"W	37.02	38
San Pedro Samuel	Tap Water	102.87	1.99	20/03/2024	42°26'34"N 3°52'39"O	59.38	38
Villasandino	Tap Water	100.56	5.91	01/04/2024	42°22'24"N 4°06'27"O	43	178
Avellanosa del Páramo	Tap Water	100.01	2.72	02/05/2024	42°27'36"N 3°52'39"O	43.76	54
Valbonilla	Tap Water	96.81	3.66	22/03/2024	42°11'53"N 4°11'11"O	99.5	40
Villanueva de Odra	Tap Water	96.20	6.29	01/04/2024	42°30'31"N 4°06'52"O	98.1	64
Santibáñez de Esgueva	Tap Water	94.83	5.04	25/04/2024	41°50'00"N 3°45'31"O	22.25	76
Villegas	Tap Water	91.99	1.43	02/04/2024	42°28'10"N 4°00'55"O	24.6	79
Bahabón de Esgueva	Tap Water	91.91	1.16	29/04/2024	41°51'43"N 3°43'45"O	21.39	84
Gumiel de Mercado	Tap Water	91.67	3.01	13/05/2024	41°45'21"N 3°48'07"O	57.71	385

Las Celadas	Tap Water	91.41	3.05	04/04/2024	42°29'02"N 3°49'42"O	27.77	20
Torrecitores del Enebral	Tap Water	91.28	4.63	21/03/2024	41°59'04"N 3°51'55"O	83.1	35
Tapia	Tap Water	85.86	5.27	26/04/2024	42°31'07"N 4°04'33"O	15	33
Pedrosa de Río Urbel	Tap Water	85.82	5.67	05/04/2024	42°24'34"N 3°49'16"O	49.06	246
Villaquirán de la Puebla	Tap Water	84.81	4.44	26/04/2024	42°16'59"N 4°06'05"O	11.48	46
Sasamón (Exp. 1)	Tap Water	83.05	1.80	09/04/2024	42°25'05"N 4°02'30"O	113.11	912
Pineda Trasmonte	Tap Water	81.14	2.30	01/04/2024	41°54'31"N 3°41'44"O	28.17	98
Fuentecén	Tap Water	79.78	0.50	15/04/2024	41°37'42"N 3°52'10"O	17.05	234
Villamayor de los Montes	Tap Water	78.37	3.48	03/04/2024	42°06'20"N 3°45'58"O	40.71	166
Solarana	Tap Water	78.26	4.88	21/03/2024	41°58'N 3°40'O	14.65	78
Nebreda	Tap Water	77.92	5.02	16/04/2024	41°58'08"N 3°38'05"O	28.43	55
Villorejo	Tap Water	76.42	4.70	22/03/2024	42°25'53"N 3°55'28"O	73.41	37
Zazuar	Tap Water	74.61	0.15	18/06/2024	41°41'45"N 3°33'18"O	313	209
Los Tremellos	Tap Water	73.20	2.37	11/04/2024	42°31'00"N 3°50'00"O	58.7	30
Manciles	Tap Water	72.56	1.79	20/03/2024	42°27'20"N 3°56'39"O	6.58	21
Vallunquera	Tap Water	71.22	1.96	29/04/2024	42°14'26"N 4°06'35"O	87.14	37
Susinos del paramo	Tap Water	67.26	0.81	22/01/2024	42°28'16"N 3°55'30"O	11.45	118
Castrojeriz	Tap Water	66.40	3.74	01/04/2024	42°17'16"N 4°08'20"O	136.08	780
Bustillo de la Vega (Palencia)	Tap Water	65.97	1.51	09/04/2024	42°27'21"N 4°44'26"O	18.99	269
Olmos de la Picaza	Tap Water	65.39	1.60	22/03/2024	42°28'50"N 3°58'46"O	54.41	16
Pedrosa del Príncipe	Tap Water	63.90	1.96	26/04/2024	42°14'57"N 4°11'56"O	28.441	164
La Parte de Bureba	Tap Water	60.81	1.28	03/05/2024	42°40'40"N 3°23'08"O	17	66
Valdeande	Tap Water	59.69	6.13	30/05/2024	42°40'40"N 3°23'08"O	30.98	99
Santibáñez Zarzaguda	Tap Water	59.68	2.22	20/03/2024	42°28'49"N 3°46'58"O	21.23	175
Aranda de Duero (Calle Pio XII)	Tap Water	58.20	2.59	05/04/2024	41°40'17"N 3°41'11"O	127.28	33 675
Campillo de Aranda	Tap Water	57.67	1.56	10/04/2024	41°36'36"N 3°43'49"O	23.92	172
Mecerreyes	Tap Water	55.59	1.83	15/04/2024	42°05'43"N 3°34'25"O	37	187

Cobos de Cerrato (Palencia)	Tap Water	55.38	0.90	04/04/2024	42°01'39"N 4°00'10"O	47	128
Madrigalejo del Monte	Tap Water	55.28	1.55	22/03/2024	42°07'28"N 3°43'30"O	25.17	176
La Nuez de Abajo	Tap Water	55.25	1.51	15/02/2024	42°27'27"N 3°48'33"O	36.31	24
Terradillos de Esgueva	Tap Water	55.08	2.76	18/06/2024	41°49'09"N 3°50'34"O	14.39	64
Villasuso	Tap Water	54.67	2.28	15/04/2024	43°04'58"N 3°19'16"O	113.17	86
Fuentemolinos	Tap Water	54.65	1.80	28/10/2024	41°36'19"N 3°50'59"O	12.81	91
Almenar de Soria	Tap Water	54.37	0.78	02/05/2024	41°40'56"N 2°11'59"O	105.99	216
Aranda de Duero (Calle San Francisco)	Tap Water	53.19	1.97	15/04/2024	41°40'43"N, 3°41'7"O	127.28	33675
Torrepadre	Tap Water	51.72	2.41	16/04/2024	42°02'37"N 3°56'13"O	28.56	67
Fuentelcésped	Tap Water	51.23	2.85	03/04/2024	41°35'28"N 3°38'26"O	22.42	275
Adrada de Haza	Tap Water	51.23	1.52	10/05/2024	41°35'39"N 3°49'18"O	10.28	205
Royuela de Río Franco	Tap Water	50.23	0.97	18/06/2024	41°59'48"N 3°57'24"O	50.61	171
Busto de Bureba	Tap Water	49.92	0.70	05/06/2024	42°39'33"N 3°15'52"O	18.56	143
Gumiel de Izán	Tap Water	48.21	1.81	20/03/2024	41°46'25"N 3°41'17"O	75.50	582
Villamayor de Treviño	Tap Water	48.17	0.66	11/04/2024	42°27'34"N 4°07'11"O	20.72	56
Lara de los Infantes	Tap Water	46.64	2.16	02/04/2024	42°07'23"N 3°26'43"O	75.85	25
La Cabañuela	Tap Water	46.15	2.14	18/06/2024	42°36'39"N 3°38'23"O	36.68	2
Olmedillo de Roa (Medida 2)	Tap Water	44.21	0.52	04/04/2024	41°46'59"N 3°56'02"O	26.03	185
Briviesca	Tap Water	41.55	0.31	20/03/2024	42°32'57"N 3°19'26"O	81.2	6547
Castromorca	Tap Water	41.54	1.33	15/05/2024	42°29'56"N 3°59'16"O	32.96	19
Cubillejo de Lara	Tap Water	36.44	1.20	16/05/2024	42°08'31"N 3°30'14"O	48.98	13
Caleruega	Tap Water	36.38	0.75	13/05/2024	41°49'32"N 3°29'13"O	47.63	387
Las Hormazas-Borcos	Tap Water	35.52	1.11	08/02/2024	42°31'00"N 3°55'00"O	19.34	19
Valverde de Miranda	Tap Water	35.27	1.10	02/04/2024	42°39'05"N 2°59'55"O	31.53	17
Cubillo del César	Tap Water	34.96	0.03	16/05/2024	42°09'07"N 3°32'28"O	62.75	30
Isar	Tap Water	32.81	1.02	05/04/2024	42°21'42"N 3°55'49"O	66.42	285

Torresandino	Tap Water	32.68	0.01	30/05/2024	41°49'46"N 3°54'36"O	93.2	573
Madrigal del Monte	Tap Water	32.50	0.53	08/07/2024	42°08'40"N 3°40'31"O	26.88	144
Quintanarraya	Tap Water	32.14	1.03	13/05/2024	41°47'12"N 3°20'18"O	153.43	126
Modúbar de San Cibrián	Tap Water	31.11	1.06	21/03/2024	42°15'10"N 3°35'11"O	87.22	80
Villandiego	Tap Water	30.81	1.00	02/04/2024	42°22'04"N 4°01'36"O	80.19	53
Sordillos	Tap Water	30.65	0.96	11/04/2024	42°27'42"N 4°06'25"O	7.73	22
Talamillo del Tozo	Tap Water	29.34	0.81	10/04/2024	42°39'00"N 3°57'53"O	55.62	19
San Pantaleón del Páramo	Tap Water	29.01	0.91	23/02/2024	42°33'52"N 3°48'13"O	16.36	12
Los Ausines	Tap Water	28.14	0.92	03/05/2024	42°13'32"N 3°35'51"O	41.68	165
Sasamón (Exp. 2)	Tap Water	27.46	0.82	03/05/2024	42°25'05"N 4°02'30"O	113.11	912
Yudego	Tap Water	27.12	0.03	30/05/2024	42°21'47"N 4°00'17"O	342.31	141
Santibáñez del Val	Tap Water	26.62	0.80	03/04/2024	41°58'26"N 3°28'50"O	14.96	70
Puentedura	Tap Water	24.99	0.00	11/04/2024	42°02'30"N 3°34'58"O	16.39	122
Los Ausines (Barrio de Sopeña)	Tap Water	23.48	0.14	20/03/2024	42°13'32"N 3°35'51"O	41.68	165
Quintanilla de la Mata	Tap Water	23.36	0.77	10/04/2024	41°59'19"N 3°46'04"O	13.80	108
Vileña de Bureba	Tap Water	23.06	0.90	09/09/2024	42°37'19"N 3°19'24"O	6.34	27
Las Hormazas-Solano	Tap Water	22.98	0.02	08/02/2024	42°31'11"N 3°55'29"O	30.83	22
Castrillo Solarana	Tap Water	22.71	0.64	03/05/2024	41°58'50"N 3°40'05"O	87.57	33
Escóbados de Arriba	Tap Water	21.99	0.67	13/05/2024	42°45'04"N 3°35'33"O	47.61	17
Marmellar de Abajo	Tap Water	21.53	0.68	04/04/2024	42°24'20"N 3°47'44"O	46.4	30
Casanova	Tap Water	21.52	0.73	18/06/2024	41°41'05"N 3°26'53"O	44.2	39
Cogollos	Tap Water	21.00	0.66	04/04/2024	42°12'03"N 3°41'56"O	31247	677
Santa María del Mercadillo	Tap Water	20.79	0.01	13/05/2024	41°51'35"N 3°33'32"O	30.21	108
Quintanilla Sobresierra	Tap Water	20.00	0.03	21/03/2024	42°34'19"N 3°42'48"O	52.87	57
Vadocondes	Tap Water	19.74	0.74	13/05/2024	41°38'22"N 3°34'25"O	25.69	363
Huermeces	Tap Water	19.49	0.10	23/02/2024	42°31'18"N 3°46'17"O	48.70	153

Peñaranda de Duero	Tap Water	16.46	0.53	26/04/2024	41°41'14"N 3°28'39"O	64.53	464
Nidáguila	Tap Water	16.20	0.57	03/04/2024	42°38'15"N 3°46'24"O	51.2	23
Quintanilla del Agua	Tap Water	15.99	0.52	25/04/2024	42°02'19"N 3°39'08"O	35.79	337
Tubilla del Lago	Tap Water	15.99	0.53	13/05/2024	41°48'05"N 3°35'11"O	23.21	172
Quintanalara	Tap Water	15.56	0.01	15/05/2024	42°10'28"N 3°32'03"O	48.93	32
Quintana del Pidio	Tap Water	14.62	0.46	16/04/2024	41°45'34"N 3°45'05"O	10.74	152
Las Hormazas-La Parte	Tap Water	14.36	0.11	08/02/2024	42°31'34"N 3°55'40"O	45.72	55
Zuzones	Tap Water	14.17	0.47	13/05/2024	41°37'21"N 3°27'28"O	274.51	97
Hoyos del Tozo	Tap Water	14.10	0.01	20/03/2024	42°42'32"N 3°56'58"O	20.33	20
San Martín de Humada	Tap Water	14.03	0.44	05/06/2024	42°39'19"N 4°02'07"O	31.6	21
Olmedillo de Roa (Medida 1)	Tap Water	13.51	0.02	01/04/2024	41°46'59"N 3°56'02"O	26.03	185
Melgar de Fernamental	Tap Water	13.47	0.39	03/04/2024	42°24'12"N 4°14'40"O	108.62	1517
Quintanilla de la Presa	Tap Water	13.18	0.02	02/04/2024	42°35'12"N 3°55'40"O	18	13
Frías	Tap Water	12.77	0.37	04/04/2024	42°45'41"N 3°17'39"O	29.38	270
Silanes	Tap Water	12.76	0.40	01/04/2024	42°40'19"N 3°10'39"O	22.7	7
Villanueva de Gumiel	Tap Water	12.66	0.45	13/05/2024	41°44'14"N 3°37'34"O	22.33	279
Los Valcárceres (Barrio de Santiago)	Tap Water	12.47	0.36	02/05/2024	42°36'58"N 3°56'06"O	23.86	25
Sarracín	Tap Water	12.43	0.38	20/03/2024	42°15'26"N 3°41'07"O	9.61	264
Fresno el Viejo (Valladolid)	Tap Water	11.92	0.03	04/04/2024	41°11'54"N 5°08'32"O	64.46	836
Cascajares de la Sierra	Tap Water	11.21	0.33	11/04/2024	42°03'42"N 3°23'58"O	13	27
Torrelara	Tap Water	11.18	0.36	16/05/2024	42°09'57"N 3°30'59"O	12.51	32
Milagros	Tap Water	10.47	0.34	02/05/2024	41°34'31"N 3°41'57"O	22.03	418
Rojas de Bureba	Tap Water	10.12	0.29	21/03/2024	42°34'39"N 3°26'27"O	24.93	58
Covarrubias	Tap Water	10.03	0.31	20/03/2024	42°03'33"N 3°31'12"O	41.07	505
Valdorros	Tap Water	9.94	0.34	25/04/2024	42°10'19"N 3°42'32"O	16.64	376
San Juan del Monte	Tap Water	9.15	0.27	02/05/2024	41°41'03"N 3°31'16"O	26.5	154

Palacios de Riopisuerga	Tap Water	9.02	0.27	13/05/2024	42°20'37"N 4°15'25"O	10.34	18
Tobes	Tap Water	9.00	0.05	25/04/2024	42°30'19"N 3°34'18"O	55.56	45
Miraveche	Tap Water	8.89	0.24	13/05/2024	42°40'28"N 3°11'58"O	22.7	95
Salinillas de Bureba	Tap Water	8.82	0.01	04/04/2024	42°33'11"N 3°23'12"O	22.83	47
Lerma	Tap Water	8.58	0.25	20/03/2024	42°01'35"N 3°45'20"O	166.4	2570
Castrillo de la Vega	Tap Water	8.16	0.27	30/05/2024	41°39'02"N 3°46'53"O	26.4	620
Quintanilla Pedro Abarca	Tap Water	7.99	0.03	23/02/2024	42°33'57"N 3°48'51"O	15.84	38
Villasuso de Mena	Tap Water	7.94	0.02	13/05/2024	43°04'58"N 3°19'16"O	349.5	86
Los Valcárceres (Barrio de San Miguel)	Tap Water	7.77	0.24	02/05/2024	42°36'58"N 3°56'06"O	23.85	25
San Esteban de Gormaz (Soria)	Tap Water	7.68	0.31	23/02/2024	41°34'24"N 3°12'18"O	406.71	2935
Fuentespina	Tap Water	7.60	0.24	13/05/2024	41°37'55"N 3°41'07"O	12.02	816
Doña Santos	Tap Water	7.35	0.05	15/05/2024	41°53'27"N 3°23'52"O	79.68	32
San Leonardo de Yagüe (Soria)	Tap Water	7.33	0.21	04/04/2024	41°49'41"N 3°04'01"O	60.58	1949
Oña	Tap Water	7.25	0.02	04/04/2024	42°44'05"N 3°24'50"O	161.4	953
Hortigüela	Tap Water	6.86	0.18	22/03/2024	42°04'05"N 3°25'31"O	20.66	107
Villela	Tap Water	6.81	0.22	21/03/2024	42°41'04"N 4°16'55"O	126.61	18
Salas de Bureba	Tap Water	6.63	0.00	04/04/2024	42°41'30"N 3°28'26"O	45729	129
Miranda de Ebro	Tap Water	6.47	0.23	25/04/2024	42°41'00"N 2°56'00"O	101.33	36025
Santa Cruz de Juarros	Tap Water	6.26	0.21	20/03/2024	41°40'43"N, 3°41'7"O	103.3	58
Anguix	Tap Water	6.22	0.17	25/04/2024	41°45'13"N 3°55'56"O	13.44	158
Orón	Tap Water	6.20	0.19	02/04/2024	42°40'06"N 2°58'56"O	180.2	221
Padrones de Bureba	Tap Water	6.20	0.15	11/04/2024	42°42'17"N 3°31'55"O	20.32	59
Saldaña de Burgos	Tap Water	6.10	0.00	15/04/2024	42°15'28"N 3°41'04"O	8.15	202
Quintanilla de las Viñas	Tap Water	6.05	0.21	03/04/2024	42°07'28"N 3°28'51"O	51.7	20
Moriana	Tap Water	5.96	0.16	15/05/2024	42°40'03"N 3°05'04"O	53.43	26

Aranda de Duero (Centro de Salud Aranda Rural)	Tap Water	5.57	0.17	02/05/2024	no sale ese centro salud	127.28	33675
Piérnigas	Tap Water	5.45	0.18	03/04/2024	42°35'24"N 3°24'46"O	13.40	39
Villavedón	Tap Water	5.40	0.17	02/05/2024	42°35'34"N 4°06'01"O	64.4	47
Montuenga	Tap Water	5.36	0.17	20/03/2024	42°09'21"N 3°44'51"O	121.6	44
Sandoval de la Reina	Tap Water	5.27	0.17	26/04/2024	42°33'32"N 4°06'19"O	26.61	37
Ura	Tap Water	5.23	0.12	15/04/2024	42°00'49"N 3°33'06"O	48.1	11
Fuencivil	Tap Water	5.23	0.17	21/03/2024	42°37'22"N 3°56'15"O	30.62	13
Quemada	Tap Water	5.21	0.17	01/04/2024	41°42'01"N 3°34'29"O	20.84	242
Piedrahita de Muñó	Tap Water	5.14	0.13	16/05/2024	42°04'33"N 3°18'30"O	51.1	8
Jaramillo Quemado	Tap Water	5.09	0.04	15/04/2024	42°05'05"N 3°21'39"O	17.45	10
Fuentenebro	Tap Water	5.01	0.15	13/05/2024	41°31'31"N 3°45'13"O	38.99	138
La Revilla	Tap Water	4.98	0.14	03/05/2024	42°00'44"N 3°19'52"O	80.03	78
Fresno de Río Tirón	Tap Water	4.98	0.15	04/04/2024	42°27'36"N 3°10'29"O	9.68	161
Villadiego	Tap Water	4.91	0.16	22/01/2024	42°30'57"N 4°00'36"O	327.96	1455
Barbadillo del Mercado	Tap Water	4.83	0.16	16/05/2024	42°02'21"N 3°21'30"O	15.19	133
Guma	Tap Water	4.80	0.00	30/05/2024	41°38'26"N 3°30'56"O	79.61	37
La Vid	Tap Water	4.77	0.16	30/05/2024	41°37'55"N 3°29'28"O	90.85	111
Noceco de Montija	Tap Water	4.55	0.09	30/05/2024	43°05'33"N 3°28'52"O	276.2	34
Cilleruelo de Bricia	Tap Water	4.28	0.09	04/04/2024	42°53'37"N 3°50'50"O	60.64	5
Moncalvillo de la sierra	Tap Water	4.13	0.03	29/04/2024	41°57'16"N 3°11'58"O	26.76	76
Poza de la Sal	Tap Water	4.05	0.11	04/04/2024	42°39'59"N 3°30'06"O	81.9	282
Revilla del Campo	Tap Water	4.03	0.09	20/03/2024	42°00'25"N 4°42'42"O	285.25	7
Villarcayo	Tap Water	3.92	0.11	12/04/2024	42°56'21"N 3°34'19"O	159.68	4043
Arcos	Tap Water	3.65	0.14	18/06/2024	42°15'58"N 3°45'20"O	31.44	1838
Grijalba	Tap Water	3.58	0.03	21/03/2024	42°25'47"N 4°07'08"O	19.75	118
Pinilla de los Moros	Tap Water	3.48	0.05	16/05/2024	42°04'04"N 3°19'38"O	11.01	33

Gredilla de Sedano	Tap Water	3.35	0.07	11/04/2024	42°43'11"N 3°43'10"O	62.79	18
Baños de Valdearados	Tap Water	3.34	0.11	03/05/2024	42°43'11"N 3°43'10"O	36.52	320
Vilviestre del Pinar	Tap Water	3.21	0.02	05/04/2024	41°57'07"N 3°04'41"O	33.89	504
Arraya de Oca	Tap Water	3.13	0.06	02/04/2024	42°24'55"N 3°23'52"O	12.25	53
Llano de Bureba	Tap Water	3.09	0.12	02/04/2024	42°37'27"N 3°27'32"O	15.18	49
Villariezo	Tap Water	3.01	0.05	26/04/2024	42°16'10"N 3°43'58"O	10.29	722
Cerezo de Río Tirón	Tap Water	3.00	0.06	01/04/2024	42°29'28"N 3°08'08"O	63.7	491
Aceña de Lara	Tap Water	2.96	0.01	16/05/2024	42°08'45"N 3°26'47"O	47.75	5
Bugedo	Tap Water	2.95	0.11	02/04/2024	42°38'57"N 3°01'04"O	9.93	191
Espinosa de los Monteros	Tap Water	2.86	0.07	05/04/2024	43°04'00"N 3°32'00"O	137.5	1648
Panizares de Valdivielso	Tap Water	2.85	0.03	11/04/2024	42°48'00"N 3°28'17"O	39.88	6
La Aguilera	Tap Water	2.76	0.10	13/05/2024	41°43'53"N 3°46'10"O	347.15	330
Mambrillas de Lara	Tap Water	2.76	0.07	16/05/2024	42°09'36"N 4°03'02"O	34.025	56
San Millán de Lara	Tap Water	2.68	0.01	16/05/2024	42°08'11"N 3°20'44"O	33.62	61
Río Quintanilla	Tap Water	2.59	0.06	04/04/2024	42°43'54"N 3°30'30"O	45.97	17
San Felices de Rudrón	Tap Water	2.53	0.07	16/04/2024	42°45'08"N 3°48'07"O	44.6	29
Jaramillo de la Fuente	Tap Water	2.48	0.02	15/05/2024	42°45'08"N 3°48'07"O	21.56	47
Rezmondo	Tap Water	2.44	0.09	18/06/2024	42°30'57"N 4°14'19"O	6.7	17
Santa Cruz de la Salceda	Tap Water	2.43	0.06	13/05/2024	41°35'41"N 3°35'41"O	25.86	147
Prádena (Segovia)	Tap Water	2.39	0.01	15/05/2024	41°08'20"N 3°41'18"O	46.33	468
Segovia	Tap Water	2.24	0.03	30/05/2024	40°56'53"N 4°07'06"O	163.59	51 525
Belorado	Tap Water	2.18	0.08	09/09/2024	42°25'14"N 3°11'25"O	133.41	1836
Huerta del Rey	Tap Water	2.18	0.06	13/05/2024	41°50'24"N 3°20'53"O	97.81	880
Rupelo	Tap Water	2.18	0.02	15/05/2024	42°07'27"N 3°23'42"O	27.51	7
Mazueco de Lara	Tap Water	2.18	0.08	25/04/2024	42°10'38"N 3°28'11"O	43.17	16
Taravero (Condado de Treviño)	Tap Water	2.11	0.08	10/04/2024	42°44'00"N 2°44'00"O	203	15

Villalmanzo	Tap Water	2.11	0.03	03/05/2024	42°02'52"N 3°44'38"O	23.91	408
Urrez	Tap Water	2.06	0.01	09/04/2024	42°16'12"N 3°24'07"O	41.33	67
Villahoz	Tap Water	2.03	0.02	04/04/2024	42°04'42"N 3°54'43"O	50.53	277
Arauzo de Miel	Tap Water	2.02	0.02	13/05/2024	41°51'36"N 3°23'16"O	57.10	272
Villoruebo	Tap Water	2.00	0.03	16/05/2024	42°10'06"N 3°26'29"O	25.75	63
Tordómar	Tap Water	1.99	0.06	26/04/2024	42°02'45"N 3°51'53"O	30.06	298
Ahedo de la Sierra	Tap Water	1.97	0.03	03/05/2024	41°59'50"N 3°21'08"O	42.62	23
Quintanar de la Sierra	Tap Water	1.96	0.04	11/04/2024	41°58'53"N 3°02'22"O	59.90	1502
Ahedo de la Sierra	Depósito	1.93	0.03	03/05/2024	41°59'50"N 3°21'08"O	42.62	23
Salas de los Infantes	Tap Water	1.85	0.02	03/04/2024	42°01'23"N 3°16'53"O	31.32	1988
Villaespasa	Tap Water	1.85	0.09	16/05/2024	42°05'56"N 3°24'08"O	19.50	22
Fresnedo	Tap Water	1.80	0.01	04/04/2024	42°59'20"N 3°32'30"O	24.49	17
Valdivielso	Tap Water	1.76	0.02	12/04/2024	42°49'29"N 3°32'49"O	129.09	403
Villalba de Duero	Tap Water	1.69	0.07	13/05/2024	41°40'56"N 3°44'42"O	13.75	709
Espinosa del Camino	Tap Water	1.64	0.04	21/03/2024	42°24'23"N 3°16'52"O	6.93	42
Fresnillo de las Dueñas	Tap Water	1.62	0.07	30/05/2024	41°38'48"N 3°38'40"O	13.69	696
Campolara	Tap Water	1.61	0.01	15/05/2024	42°07'10"N 3°25'38"O	13.24	48
Logroño (La Rioja)	Tap Water	1.51	0.03	03/04/2024	42°28'12"N 2°26'44"O	79.55	151164
Cardeñadijo	Tap Water	1.50	0.03	12/04/2024	42°18'05"N 3°40'01"O	9.21	1430
Zael	Tap Water	1.33	0.04	01/04/2024	42°06'34"N 3°49'26"O	338	116
Villaverde Mogina	Tap Water	1.22	0.01	04/04/2024	42°09'36"N 4°03'02"O	13.55	75
Sotopalacios	Tap Water	1.21	0.01	01/04/2024	42°26'11"N 3°40'45"O	346.05	568
Quintanilla Cabrera	Tap Water	1.21	0.04	16/05/2024	42°10'02"N 3°24'47"O	12.15	11
Rabé de las Calzadas	Tap Water	1.18	0.01	04/04/2024	42°20'24"N 3°50'03"O	10.107	254
Tardajos	Tap Water	1.16	0.03	01/04/2024	42°20'50"N 3°49'09"O	12.8	864
Iglesiapinta	Tap Water	1.16	0.03	15/05/2024	42°08'58"N 3°19'27"O	21.43	29

Arlanzón	Tap Water	1.09	0.01	01/04/2024	42°19'22"N 3°27'29"O	77.74	427
Arcones (Segovia)	Tap Water	1.05	0.00	15/05/2024	41°07'07"N 3°43'27"O	31.75	180
Atapuerca	Tap Water	1.04	0.11	20/03/2024	42°22'36"N 3°30'33"O	24.75	182
Vizcaínos	Tap Water	1.04	0.01	16/05/2024	42°06'05"N 3°16'01"O	11.48	40
Vivar del Cid	Tap Water	1.00	0.04	21/03/2024	42°25'19"N 3°40'46"O	140.04	239
Burgos (Calle Laín Calvo)	Tap Water	0.99	0.03	20/03/2024	42°20'27"N 3°41'59"O	107.08	176 551
Cortes (Barrio)	Tap Water	0.99	0.03	26/04/2024	42°19'42"N 3°39'52"O	109	1012
Villas del Arlanzón (Villalbilla de Burgos)	Tap Water	0.93	0.02	21/03/2024	42°20'49"N 3°46'45"O	14.44	1522
Cañizar de Argaño	Tap Water	0.91	0.02	21/03/2024	42°24'16"N 3°56'42"O	13.16	90
San Martín de Ubierna	Tap Water	0.86	0.02	12/04/2024	42°30'23"N 3°42'25"O	43.43	37
Agés	Tap Water	0.83	0.01	21/03/2024	42°22'11"N 3°28'46"O	16.12	56
Santa María del Campo	Tap Water	0.80	0.01	12/04/2024	42°07'55"N 3°58'27"O	60.32	523
Tinieblas de la Sierra	Tap Water	0.80	0.03	02/04/2024	42°10'21"N 3°21'47"O	29.38	23
Villagonzalo Pedernales	Tap Water	0.79	0.02	05/04/2024	42°10'21"N 3°21'47"O	13.76	1879
Olmos de Atapuerca	Tap Water	0.75	0.02	09/04/2024	42°23'29"N 3°31'56"O	89.26	57
Fresno de Rodilla	Tap Water	0.74	0.01	18/06/2024	42°25'12"N 3°29'06"O	12.146	49
Paúles de Lara	Tap Water	0.71	0.01	03/04/2024	42°09'00"N 3°28'00"O	41.31	11
Palacios de la Sierra	Tap Water	0.69	0.01	25/04/2024	41°57'48"N 3°07'34"O	70.4	677
Presencio	Tap Water	0.68	0.06	20/03/2024	42°11'14"N 3°54'01"O	35.35	208
Arroyal de Vivar	Tap Water	0.60	0.03	03/04/2024	42°24'43"N 3°44'58"O	47.69	157
Villanueva Río Ubierna	Tap Water	0.58	0.04	09/09/2024	42°26'05"N 3°43'36"O	74.17	62
Santa Coloma del Rudrón	Tap Water	0.52	0.01	08/07/2024	42°41'15"N 3°52'38"O	19.41	12
Tañabueyes	Tap Water	0.38	0.01	16/05/2024	42°09'00"N 3°22'58"O	26.62	18
Monterrubio de la Demanda	Tap Water	0.14	0.02	06/06/2024	42°08'53"N 3°06'45"O	15.11	56

Table S2. Citizen Science Project Results: Nitrate Concentration in Spring Water Samples

SPRING WATER SAMPLES (SUMMARY)				
	Nº of samples	**%**		
TOTAL	155	100		
> 50 mg L^{-1}	66	43		
> 30 mg L^{-1}	83	54		
> 10 mg L^{-1}	109	70		

SPRING WATER SAMPLES				
Town	**Source**	**Nitrate Concentration (mg L^{-1})**	**Standard Error**	**Date of Analysis**
Arraya de Oca	Fuente "Los Pilones" (Prallorente)	145.20	5.42	25/04/2024
Olmillos (Soria)	Fuente "El Santo"	127.92	2.40	03/05/2024
Piedrahita de Juarros	Fuente "Año 1886"	125.83	3.43	25/04/2024
Pineda Trasmonte	Fuente del Corcho	120.67	3.65	01/04/2024
Santibáñez de Esgueva	Fuente "del Caño"	119.64	3.56	10/05/2024
Villamayor de Treviño	Fuente	115.09	3.18	11/04/2024
Olmedillo de Roa	Fuente (derecha)	106.62	6.30	02/04/2024
Villagonzalo Pedernales	Fuente Plaza Mayor	100.09	4.00	20/03/2024
Villatuelda	Fuente de abajo	98.22	5.38	05/04/2024
Ibeas de Juarros	Fuente	94.51	5.82	09/04/2024
Santibáñez de Esgueva	Fuente "de los Pilones"	92.62	1.28	10/05/2024
Santibáñez de Esgueva	Fuente "de Henosa"	91.36	2.47	10/05/2024
Turrientes	Fuente iglesia	89.82	2.70	09/04/2024
Santibáñez de Esgueva	Fuente "Valdefuentes"	87.30	1.92	10/05/2024
Pedrosa de Río Urbel	Fuente Pública	86.94	0.65	05/04/2024
Santibáñez de Esgueva	Fuente "de la Peña Hueca"	85.83	1.98	10/05/2024
Valdorros	Fuente "Caño viejo"	83.32	2.66	20/03/2024
Valdorros	Fuente (caño)	83.32	2.66	26/04/2024
Avellanosa del páramo	Fuente de la bola	81.62	1.91	22/01/2024
Villamayor de los Montes	Fuente carretera Zael S/N	81.09	3.62	10/04/2024
Villasandino	Fuente	79.97	1.86	01/04/2024
Santibáñez de Esgueva	Fuente "Valdequintana"	79.77	3.11	10/05/2024
Tapia	Fuente	79.69	1.00	26/04/2024
San Martín de Rubiales	Fuente	79.63	0.72	21/03/2024
Briviesca	Fuente Valdequintanilla	79.43	2.13	04/04/2024
Bahabón de Esgueva	Fuente "el Caño"	78.48	2.87	29/04/2024
Fuentelcésped	Fuente	78.21	2.16	03/04/2024
Yudego	Manantial zona huertas	78.10	2.12	30/05/2024
Sarracín	Fuente	78.08	3.50	09/04/2024
Villalmanzo	Fuente (natural)	77.55	2.10	03/05/2024
Torresandino	Fuente San Pedro	76.97	1.05	30/05/2024

Vallunquera	Fuente	75.90	2.04	10/04/2024
Quintanapalla	Fuente (caño lateral)	75.68	5.40	25/04/2024
Solarana	Fuente plaza	75.63	2.11	10/04/2024
Villamayor de los Montes	Fuente mayor	75.18	4.84	02/04/2024
Quintanapalla	Fuente "abovedada dos caños"	74.74	2.84	25/04/2024
Sandoval de la Reina	Fuente	72.98	2.46	26/04/2024
Almenar de Soria	Fuente	72.65	4.51	02/05/2024
Olmos de la Picaza	Fuente	69.29	3.34	25/04/2024
Cerratón de Juarros	Fuente publica	68.86	3.20	09/04/2024
Castrojeriz (carretera)	Fuente "Mortero"	67.82	2.14	10/05/2024
Pedrosa de Muñó	Fuente	67.22	2.92	09/04/2024
Torresandino	Fuente vieja	66.77	2.08	21/03/2024
Vallunquera	Fuente "La Bodeguilla"	65.24	2.21	10/05/2024
Villahoz	Fuente "de las Pilas"	58.87	3.41	16/04/2024
Peñaranda de Duero	Fuente	58.76	0.88	11/04/2024
Tardajos	Fuente la Cambija	58.66	0.92	21/03/2024
Bahabón de Esgueva	Fuente "los Cañales"	56.63	1.54	29/04/2024
Tobar	Fuente carretera	56.57	0.81	22/01/2024
Cobos de Cerrato (Palencia)	Fuente del Pilón	56.39	0.32	03/04/2024
Frandovínez	Fuente pequeña	55.53	0.45	25/04/2024
Royuela de Río Franco	Fuente "Calle de Abajo"	55.53	0.77	29/04/2024
Torrepadre	Fuente "La Morita"	55.27	2.15	16/04/2024
Villahoz	Fuente "Carretera"	55.05	3.08	16/04/2024
San Juan de Ortega	Fuente-Pilon del Caño	54.78	1.59	10/04/2024
Quintanilla del Monte en Juarros	Fuente (pilón camino monte)	53.71	3.17	25/04/2024
Torrepadre	Fuente "El Charcón"	52.32	1.95	16/04/2024
Villaldemiro	Fuente	51.91	2.24	21/03/2024
Villaescusa la Solana	Fuente (pilón)	51.78	0.44	25/04/2024
Buniel	Fuente	49.05	1.56	03/04/2024
Taravero-Condado de Treviño	Fuente	48.99	1.56	10/04/2024
Ros (Valle de Santibáñez)	Fuente	48.87	2.74	02/05/2024
Covarrubias	Fuente Cerezuelos	46.81	1.42	15/04/2024
Anguix	Fuente	44.08	2.34	25/04/2024
Santovenia de Oca	Fuente 2 caños	42.93	0.34	10/04/2024
Ruyales del Páramo	Fuente	42.83	0.58	23/02/2024
Espinosa del Camino	Fuente el Cozarro	42.66	1.14	10/04/2024
Rabé de las Calzadas	Fuente del Peregrino	40.00	0.35	22/03/2024
Olmillos de San Esteban	"Fuente 2"	39.34	1.32	26/04/2024
Olmillos de San Esteban	"Fuente 1"	37.86	1.55	26/04/2024
Adrada de Haza	Fuente "de Carrehón Hangas"	37.80	2.03	10/05/2024
Arroyal de Vivar	Fuente	36.29	1.25	02/04/2024
Cartuja de Miraflores (Burgos)	Fuente "de la Teja"	34.22	1.05	26/04/2024

Torrepadre	Fuente "Los Caños"	34.10	1.08	16/04/2024
Mambrillas de Lara	Fuente "Vieja"	33.38	1.07	16/05/2024
Escobados de Arriba	Fuente de la Plaza	30.72	1.04	13/05/2024
Villaescusa la Sombría	Fuente "Dos Caños"	30.67	0.97	25/04/2024
Adrada de Haza	Fuente de la Salud	30.89	1.01	12/11/2024
Aranda de Duero	Fuente	29.07	0.02	30/05/2024
Escobados de Arriba	Abrevadero (pilón 2)	28.41	0.95	13/05/2024
Adrada de Haza	Fuente "del Puente/ del Hambre"	28.13	0.90	13/05/2024
Villandiego	Fuente	26.72	0.85	02/04/2024
Briviesca	Fuente Castrotoño	26.10	0.21	04/04/2024
Villavedón	Fuente	24.98	0.01	02/05/2024
Baños de Valdearados	Fuente	24.49	0.76	03/05/2024
Villamayor de los Montes	Fuente Alameda	23.12	0.02	10/04/2024
Rabé de las Calzadas	Fuente (Plaza) Cuatro Caños	22.51	0.80	22/03/2024
Frandovínez	Fuente grande	21.47	0.03	25/04/2024
Quintanalara	Fuente	19.37	0.64	16/05/2024
Ordejón de abajo	Fuente	18.20	0.49	10/04/2024
Doña Santos	Fuente	18.06	0.03	15/05/2024
Cañizar de Argaño	Fuente	17.50	0.56	21/03/2024
Santa Casilda (Santuario)	Fuente	15.94	0.46	04/04/2024
Quintanilla Pedro Abarca	Fuente	15.67	0.03	23/02/2024
Hoyos del Tozo	Fuente	14.60	0.48	20/03/2024
Santibáñez del Val	Fuente	14.40	0.03	03/04/2024
Quintanilla de la Presa	Fuente	13.68	0.43	02/04/2024
Torrelara	Fuente	13.62	0.35	16/05/2024
Villadiego	Fuente "Pozo Artesiano"	12.57	0.31	22/01/2024
San Martín de Ubierna	Fuente	12.17	0.37	12/04/2024
Lara de los Infantes	Fuente "Romana"	11.93	0.28	16/05/2024
Lara de los Infantes	Fuente "la Campana"	11.74	0.35	16/05/2024
Santa María del Invierno	Fuente	9.64	0.32	25/04/2024
Escobados de Arriba	Pilón 1	9.61	0.30	13/05/2024
Madrigalejo del Monte	Fuente (Plaza)	9.05	0.39	22/03/2024
Los Valcárceres (Barrio de San Miguel)	Fuente	8.56	0.26	02/05/2024
Cubillo del César	Fuente "el Caño"	7.89	0.24	16/05/2024
Villela	Fuente	7.46	0.20	21/03/2024
Vilviestre del Pinar	Fuente Agua de la Solana	7.18	0.07	09/04/2024
Miranda de Ebro	Fuente Plaza del Mercado	7.08	0.23	16/04/2024
Tinieblas de la Sierra	Fuente	6.85	0.00	02/04/2024
Quintanilla Sobresierra	Fuente	6.81	0.02	21/03/2024
Poza de la Sal	Fuente	6.59	0.01	03/04/2024
Orón	Fuente	5.89	0.00	02/04/2024

Santa Olalla de Bureba	Manantial Villasuso Manadera	5.47	0.16	15/04/2024
Santa Cruz de Juarros	Fuente	4.87	0.17	09/04/2024
La Sía	Fuente	4.87	0.11	05/04/2024
Aceña de Lara	Fuente	4.60	0.01	16/05/2024
Villafranca Montes de Oca	Fuente	4.58	0.08	04/04/2024
Lara de los Infantes	Fuente	4.29	0.08	02/04/2024
Villanueva de Tovera (Condado de Treviño)	Fuente pública	4.07	0.12	10/04/2024
Palacios de la Sierra	Fuente Campana	3.86	0.13	25/04/2024
Valverde de Miranda	Fuente	3.86	0.10	02/04/2024
Saldaña de Burgos	Fuente (pilón)	3.79	0.05	15/04/2024
Vilviestre del Pinar	Fuente Las Canales	3.36	0.01	05/04/2024
Palacios de la Sierra	Fuente Cardosa	3.31	0.06	25/04/2024
Cerezo de Río Tirón	Fuente	3.12	0.03	01/04/2024
Santa Olalla de Bureba	Fuente	2.73	0.06	04/04/2024
Bugedo	Fuente	2.70	0.04	02/04/2024
Rupelo	Fuente	2.65	0.01	15/05/2024
Olmillos (Soria)	Fuente "El Pozo"	2.19	0.01	03/05/2024
Urrez	Fuente	2.13	0.02	09/04/2024
Moncalvillo de la sierra	Fuente	2.12	0.04	29/04/2024
Pinarejos	Fuente	2.02	0.01	15/05/2024
Turrientes	Fuente	1.66	0.03	09/04/2024
Jaramillo de la Fuente	Fuente	1.64	0.05	15/05/2024
Vega de Lara	Fuente	1.64	0.04	16/05/2024
Zael	Fuente	1.39	0.02	02/04/2024
Aceña de Lara	Fuente Sur	1.18	0.03	16/05/2024
Bustillo de la Vega (Palencia)	Fuente "Caño"	1.17	0.03	09/04/2024
Cuevas de San Clemente	Fuente	1.14	0.04	20/03/2024
Campolara	Fuente	1.10	0.02	15/05/2024
Lerma	Fuente del cura	1.08	0.04	02/04/2024
Barbadillo del Pez	Fuente "el Molino"	1.00	0.02	15/05/2024
Vivar del Cid	Fuente	0.96	0.02	21/03/2024
La Nuez de Abajo	Fuente Cantina	0.86	0.05	23/02/2024
Villafranca de Oca	Fuente Ermita	0.85	0.03	02/04/2024
Iglesiapinta	Fuente	0.76	0.01	15/05/2024

Table 3. Citizen Science Project Results: Nitrate Concentration in Other Water Sources

OTHER WATER SOURCES (SUMMARY)				
	Nº of samples	%		
TOTAL	53	100		
> 50 mg L^{-1}	22	42		
> 30 mg L^{-1}	27	51		
> 10 mg L^{-1}	38	72		

OTHER WATER SOURCES				
Town	**Source**	**Nitrate Concentration (mg L^{-1})**	**Standard Error**	**Date of Analysis**
Los Balbases	Well (PP)	136.12	9.24	12/04/2024
Las Celadas (Groundwater spring “Ontoria”)	River	110.67	3.49	04/04/2024
Las Celadas (Groundwater spring “Conejera”)	River	108.01	2.56	05/04/2024
Quintanilla de Riofresno	Municipal Water Reservoir	106.03	3.18	11/04/2024
Humienta	Spring	103.90	3.26	10/04/2024
Zael	Well	90.55	2.36	02/04/2024
Humienta	River	85.67	2.62	02/05/2024
Villasandino	Well	85.32	1.11	21/03/2024
Pineda Trasmonte	Stream	79.97	3.76	01/04/2024
Pineda Trasmonte	River	65.44	1.78	01/04/2024
Villamayor de los Montes	Well	59.48	1.76	02/04/2024
Arraya de Oca	River of the Urban Springs	57.35	3.25	02/04/2024
Valdorros	Well	53.93	2.75	20/03/2024
Covarrubias	Well	51.94	0.20	20/03/2024
Bustillo de la Vega (Palencia)	Well	45.28	1.29	09/04/2024
Madrigalejo del Monte	Farm	33.90	1.06	22/03/2024
Villamayor de los Montes	Reverse osmosis tap	31.46	0.02	04/04/2024
Humienta	Well	27.58	0.02	03/05/2024
Quintanilla de la Presa	River	22.33	0.72	02/04/2024
Hontoria de la Cantera	River	20.15	0.66	01/04/2024
Cardeñadijo	Well	19.07	0.11	21/03/2024
La Nuez de Abajo	Reverse osmosis tap	18.26	1.17	23/02/2024
Briviesca	Reverse osmosis tap	16.01	0.52	09/04/2024
Orón	River Oroncillo	15.07	0.49	02/04/2024
AquaBona	Bottled	12.45	0.01	03/05/2024
AguaDoy	Bottled	12.33	0.40	16/04/2024

Cardeñadijo	Municipal Water Reservoirs	11.94	0.33	21/03/2024
Los Tremellos	Well Vegetable Garden	10.54	0.08	04/04/2024
San Martín de Rubiales	Tap Water (filtered)	6.40	0.01	10/04/2024
Ordejón de abajo	Municipal Water Reservoir	5.79	0.17	10/04/2024
Cubillo del Campo	River	4.71	0.08	01/04/2024
Quintanilla de Riofresno	Well	4.55	0.10	11/04/2024
Briviesca	Municipal Water Reservoir Valdequintanilla	3.94	0.10	04/04/2024
Olmillos de Atapuerca	River	3.60	0.05	09/04/2024

S2. Quantification of Nitrate Concentration in tap water samples

Stock solutions: A stock nitrate solution was prepared by dissolving 0.722 g of potassium nitrate (KNO_3) in Milli-Q water, adding 2 mL of chloroform ($CHCl_3$) as preservative, and making up to 1 L. An intermediate nitrate solution was prepared by diluting 100 mL of the stock nitrate solution to 1 L with Milli-Q water and adding 2 mL of $CHCl_3$. A 1M hydrochloric acid (HCl) solution was also prepared by diluting 83 mL of concentrated HCl (37%) to 1 L with Milli-Q water.

Calibration standards: Solutions were prepared in 50 mL volumetric flasks by mixing 1 mL of the HCl solution with varying volumes (0, 1, 5, 10, 20, 30, 40 mL) of the intermediate nitrate solution and diluting to volume with Milli-Q water. The blank contained only 1 mL of HCl and Milli-Q water.

For nitrate measurements in real water samples, 0.5 mL of the HCl solution was added to 25 mL volumetric flasks, followed by real water sample addition to the mark. Absorbance was measured at 220 nm using a UV-Vis spectrophotometer with 1 cm quartz cuvettes. Samples were diluted with Milli-Q water as necessary to remain within the calibration range. No correction at 275 nm was applied, as the samples were assumed to have low organic matter content.

S3. Synthesis of the polymer FNO_3 and characterization by FTIR, TGA and DSC

The polymer FNO_3 was synthesized via bulk radical polymerization of 1-vinyl-2-pyrrolidone (VP), methyl methacrylate (MMA), (vinylbenzyl)trimethylammonium chloride (NNZA), and 6-methoxy-1-(pent-4-en-1-yl)quinolin-1-ium bromide (SA-R1025), using ethylene glycol dimethacrylate (EGDMMA) as a cross-linking agent. The co-monomer molar ratio was VP/MMA/NNZA/SA-R1025/EGDMMA = 24/25/49.75/0.25/1. A photochemical radical initiator, 2,2-dimethoxy-2-phenylacetophenone (1.56 wt%), was employed. Polymerization was carried out overnight under 365 nm light irradiation, in an oxygen-free environment, within a silanized glass mold of 200 µm thickness. From this film, circular discs of fixed diameter were subsequently punched out in order to ensure reproducibility in the experimental assays.

To gain insight into the physicochemical properties of the FNO_3 polymer, Figure S1 compiles its basic characterization. Panel (a) displays a schematic representation of the polymer structure, highlighting the presence of functional moieties. Panel (b) shows the FT-IR spectrum, where the characteristic vibrational bands corresponding to the polymer backbone and functional groups can be observed. Panel (c) presents the thermogravimetric analysis (TGA) curve obtained at a heating rate of 10 $°C \cdot min^{-1}$ under nitrogen atmosphere, from which the decomposition onset temperatures (T_5 and T_{10}) were extracted. Panel (d) includes the differential scanning calorimetry (DSC) results; however, no clear glass transition temperature (Tg) was detected, likely due to a Tg value below the sensitivity limit of the instrument. The DSC analysis was carried out using the following thermal cycle: equilibration at –80 °C, followed by a heating ramp of 10 $°C \cdot min^{-1}$ up to 250 °C (cycle 1), cooling back to –80 °C, and a second identical heating cycle to ensure reproducibility.

The TGA curve indicates that the temperature at 5% weight loss (T_5) was approximately 250 °C, and 10% weight loss (T_{10}) occurred at 270 °C, indicating the initial stages of thermal degradation. The degradation profile exhibits a two-step weight loss process. The first event, starting near 250 °C, is attributed to the decomposition and volatilization of the side chains. These moieties, being relatively short and of lower molecular weight than the polymer backbone, degrade into small, volatile fragments that are easily released upon heating. This early volatilization contributes significantly to the observed T_5 and T_{10} values. The second weight loss above 350 °C corresponds to the decomposition of the main polymer chain, which generates higher molecular weight fragments that require higher temperatures to volatilize. Small residual mass beyond 600 °C suggests the presence of char or thermally stable residues, likely originating from the ionic components. Overall, the polymer exhibits sufficient thermal stability for applications in aqueous environments, with degradation initiating well above typical operating temperatures.

The FTIR spectrum of the copolymer confirms the presence of the expected functional groups. A broad band centered at 3366 cm^{-1}, with a shoulder at 3255 cm^{-1}, is attributed to N–H stretching vibrations from the pyrrolidone ring (VP). The peaks at 3015 cm^{-1} and 2951 cm^{-1} correspond to aromatic and aliphatic C–H stretching vibrations. The strong absorption at 1718 cm^{-1} confirms the presence of ester C=O stretching from MMA and the crosslinker units, while the band at 1665 cm^{-1} is assigned to amide C=O stretching from VP. A clear band at 1478 cm^{-1} can be ascribed to aliphatic carbons bending vibrations. Finally, peaks at 976 cm^{-1}, 896 cm^{-1}, and 821 cm^{-1} are characteristic of out-of-plane C–H bending in substituted aromatic rings and heterocyclic moieties (imidazolium, quinolinium). This analysis confirms the successful incorporation of all key monomeric units into the copolymer backbone.

To complement the above characterization, the polymeric film was found to have a thickness of 176 μm, slightly lower than the 200 μm thickness of the mold. This difference is due to the solvent required to properly dissolve the starting monomers, which is subsequently removed during polymer washing. Morphologically, the material is dense and non-porous. In response to reviewer comments, the mechanical properties of the FNO_3 films were measured, yielding a Young’s modulus of 49 ± 2 MPa.

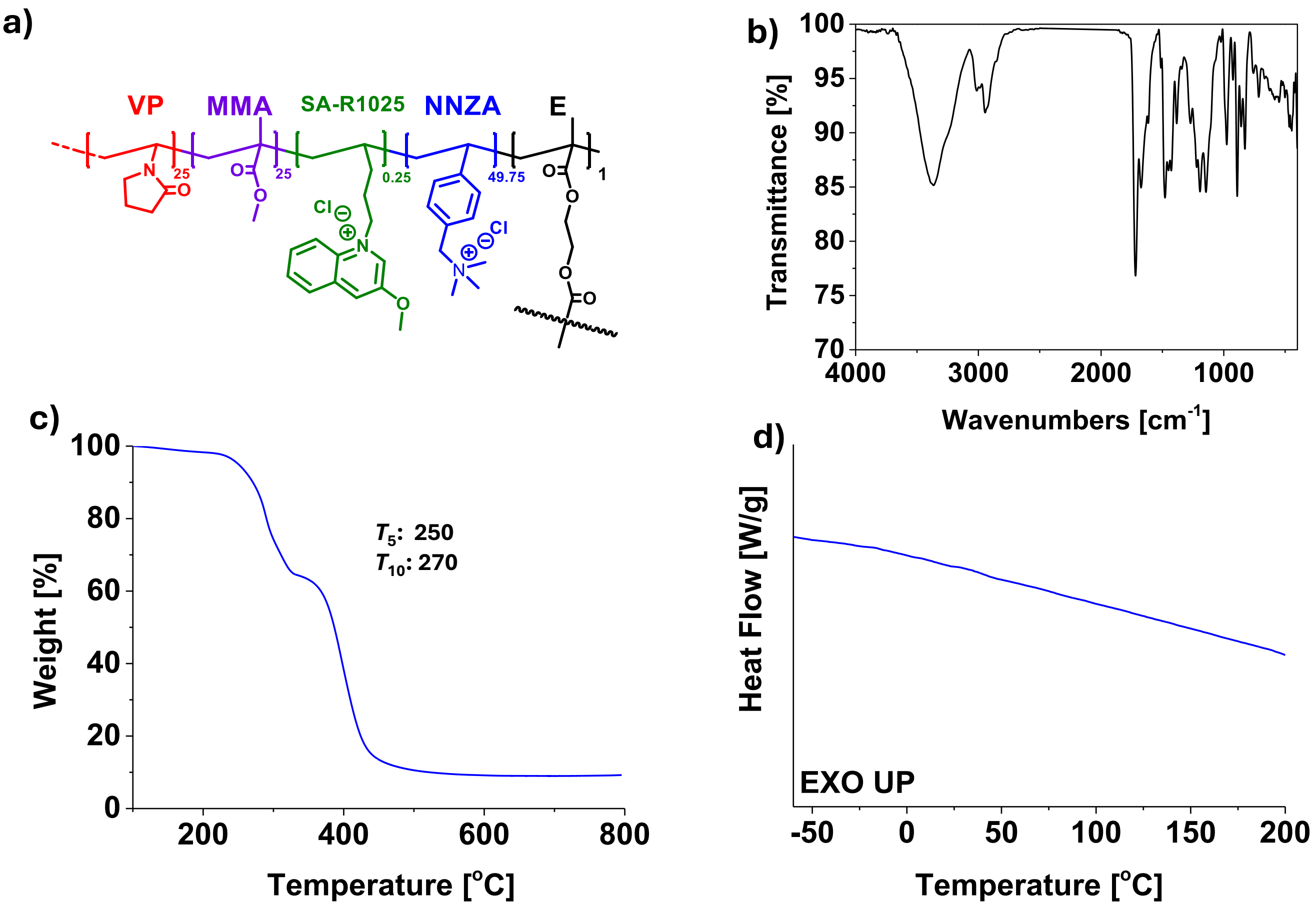

Figure S1. FNO_3 Polymer (**a**) characterization by (**b**) FT-IR, Figure shows the IR spectra of the polymer; (**c**) Thermogravimetric curve at 10°C·min^{-1} under nitrogen atmosphere showing T_5 and T_{10} temperatures; (**d**) DSC curve at a heating rate of 20°C·min^{-1} under nitrogen atmosphere.

S4. Synthesis of the sensory monomer 6-methoxy-1-(pent-4-en-1-yl)quinolin-1-ium bromide (SA-R1025)

In a sealed pressure tube, 345 mg (2.17 mmol) of 6-methoxyquinoline and 365 mg (2.45 mmol) of 5-bromopent-1-ene were added sequentially. The tube was wrapped in aluminum foil to protect the reaction from light and then heated at 70 °C overnight under magnetic stirring. After cooling to room temperature, 5–10 mL of diethyl ether were added, and the mixture was manually shaken to facilitate washing. This ether washing step was repeated two more times. The remaining viscous residue was redissolved in 5–10 mL of methanol and precipitated by the addition of 150 mL of diethyl ether. The resulting solid was collected by filtration and dried under vacuum. Yield: 80%.

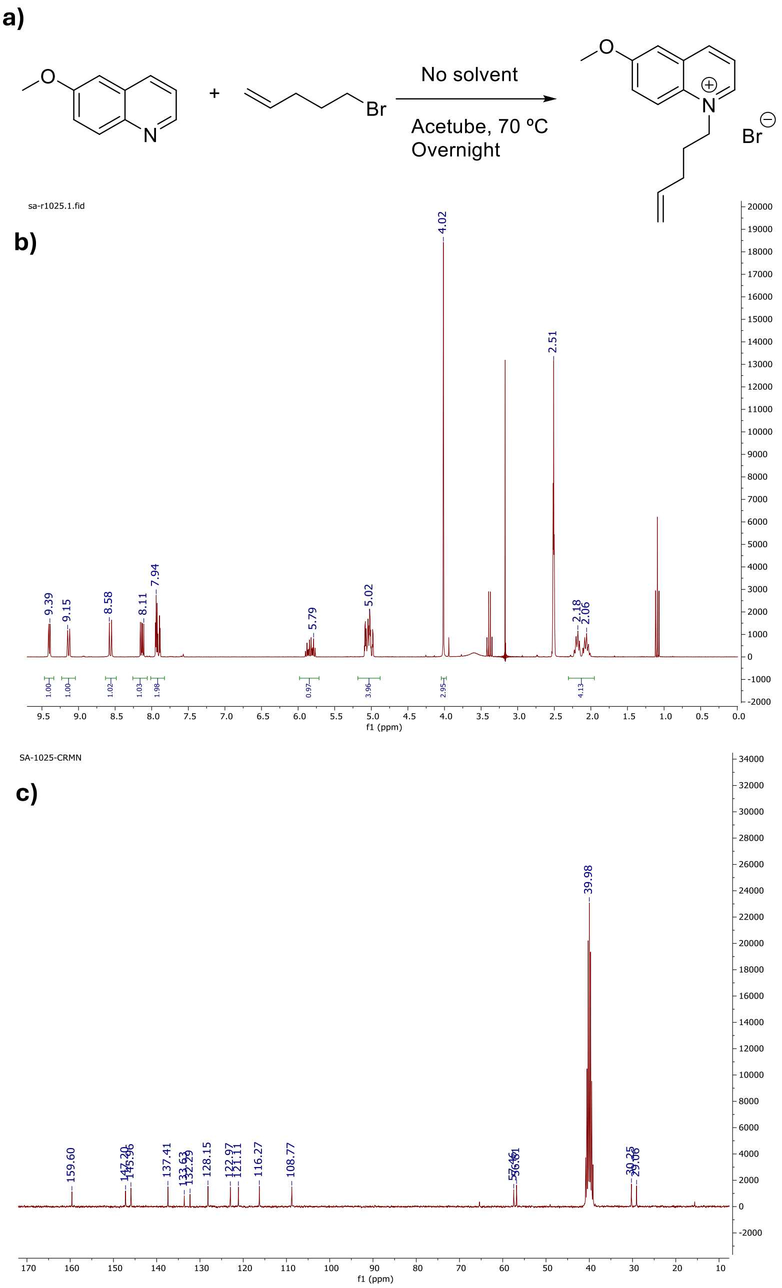

Figure S2. a) Reaction scheme for the synthesis of SA-R1025 via quaternization of 6-methoxyquinoline with 5-bromopent-1-ene. b)1H-NMR spectrum recorded in DMSO-d_6 at 300 MHz. C) 13C-NMR spectrum recorded in DMSO-d_6 at 75 MHz.

S5. Sorption study

The adsorption process in solution involves several sequential transport stages:

1. External transport of the solute from the bulk solution to the boundary layer surrounding the adsorbent.
2. Diffusion of the solute through the interface to the adsorbent surface, also known as external mass transfer.
3. Intraparticle diffusion.
4. Actual adsorption onto the active sites.

Two mathematical modeling approaches were employed for the kinetic study of adsorption:

- Surface Reaction Model (SRM), which assumes rapid mass transfer and that the adsorption reaction (step 4) is the rate-limiting step.
- Mass Transfer Reaction Model (MTM), where mass transfer is the slow step and adsorption reaction is fast. This approach may involve a single-resistance model (step 2 or 3) or a dual-resistance model, where diffusion processes (steps 2 and 3) control the rate.

An inherent limitation of both modeling approaches (SRM and MTM) is that the apparent numerical value of a rate parameter obtained by fitting the model to experimental data may not represent its true intrinsic value. Instead, it can be an aggregate parameter that incorporates the effects of other processes not explicitly considered in the model derivation. However, if a model proves inapplicable, this invalidates its fundamental assumptions.

Prior to developing the two models, it is essential to establish the mass balance, the differential form of which is given by Equation (1).

$$V\frac{dC_t}{dt} + M\frac{dq_t}{dt} = 0 \quad (1)$$

By integrating Equation (1) and rearranging, Equation (2) is obtained.

$$q_t = (C_o - C_t)\frac{V}{M} \quad (2)$$

Where q_t represents the milligrams of adsorbate per gram of adsorbent at time t, C_o and C_t denote the initial and time-t concentrations of adsorbate in milligrams per liter, respectively, V is the volume of the solution in liters, and M is the mass of the adsorbent in grams.

a) Surface Reaction Model (SRM)

The adsorption reaction can be described using the following scheme:

$$NO_3^- + S^* \underset{k_d}{\overset{k_a}{\rightleftharpoons}} S\text{-}NO_3$$

Where S^* represents the active sites on the material where nitrate binds, k_a is the second-order adsorption rate constant, and k_d is the first-order desorption rate constant. The rate equation corresponding to the above scheme is expressed as Equation (3):

$$\frac{dq_t}{dt} = k_a C_t (q_m - q_t) - k_d q_t \quad (3)$$

Equation (3) is also referred to as the Langmuir kinetics equation, as it reduces to the Langmuir isotherm equation at equilibrium, where $dq_e/dt=0$.

C_t is the concentration of adsorbate present in the solution at time ttt, which can be calculated as $C_t = C_o - q_t M/V$. Depending on the amount adsorbed, the integrated rate equation leads to two different scenarios, as described by Azizian (Azizian, 2004). When $C_o >> q_t M/V$, the substrate concentration can be considered constant and equal to the initial concentration, resulting in a pseudo-first-order equation, as expressed in Equation (4).

$$q_t = q_e\left(1 - e^{-k_1 t}\right) \quad (4)$$

Conversely, if the previous assumption cannot be made, the integration of Equation (3) leads to a pseudo-second-order equation, as shown in Equation (5).

$$q_t = \frac{1 + k_2 q_e t}{k_2 q_e^2} \quad (5)$$

The kinetic study was conducted in 3.5 mL of solution, with nitrate concentrations ranging from 5 to 90 ppm and in the presence of 0.0016 g of adsorbent. The adsorption percentage ranged between 51% and 86%, meaning that q_tM/V is not negligible compared to C_o. Therefore, the experimental data are expected to fit a pseudo-second-order reaction, as described by Equation (5).

By fitting the qt values to equation (5), Figure S3 is obtained. As observed, the equation does not fit the experimental data points. At this stage, it can be concluded that the SRM model does not adequately describe the observed behavior, thereby invalidating its underlying hypothesis.

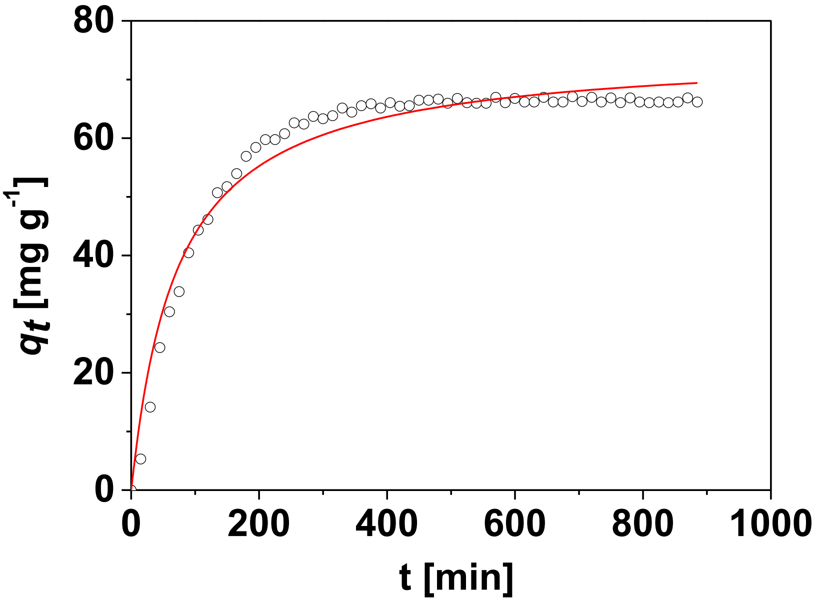

Figure S3: Pseudo-second-order SRM model fitted to the adsorption kinetics at 40 ppm and 25°C.

b) Mass Transfer Reaction Model (MTR).

In this mathematical model, the kinetic process is controlled by diffusion stages, where either one or both stages may govern the reaction rate. Therefore, it is essential to first consider the two types of mass transfer: diffusion through the external film and intraparticle diffusion.

Diffusion through the external film is modeled based on a linear driving force, which assumes that the mass transfer rate depends linearly on the concentration difference between the bulk solution and the concentration at the external surface of the adsorbent:

$$\frac{\partial q_t}{\partial t} = k_f S_A (C_t - C_i) \quad (6)$$

Where k_f is the external or film mass transfer coefficient, S_A is the specific surface area of the adsorbent, and C_t and C_i represent the adsorbate concentrations in the solution at time t and at the surface in equilibrium with the solid phase concentration, q, respectively. For intraparticle diffusion, the model assumes a uniform membrane of thickness lll, through which the solute diffuses with a constant diffusivity D_s. Fick's law of diffusion for this system is expressed by Equation (7).

$$\frac{\partial q_t}{\partial t} = D_s\left(\frac{\partial^2 q_t}{\partial x^2}\right) \quad (7)$$

b1) Single Resistance Model: Intraparticle Diffusion.

In this model, it is assumed that diffusion occurs within a homogeneous solution of limited volume. The solute concentration in the solution is always uniform and initially equal to C_o,while the initial concentration within the membrane is zero. The membrane has a thickness of 2l, occupying the spatial domain $-l \leq x \leq l$, whereas the solution is confined to the regions $-l-a \leq x \leq -l$, $l \leq x \leq l+a$. Crank provides the analytical solution, assuming that intraparticle diffusion is the sole rate-controlling step (Crank, 1979).

$$\frac{q_t}{q_e} = 1 - \sum_{n=1}^{\infty} \frac{2\alpha(1+\alpha)}{1+\alpha+\alpha^2\gamma_n^2} \exp\left(-\frac{D_s\gamma_n^2 t}{l^2}\right) \quad (8)$$

Where γ_n are the positive non-zero roots of:

$$tan\,\gamma_n = -\alpha\ \gamma_n \quad (9)$$

The parameter α denotes the ratio of the solution volume to the membrane volume and can be determined by Equation (10).

$$\frac{Mq_e}{2aC_o} = \frac{1}{1+\alpha} \quad (10)$$

Where a is the volume of the solution. Once α is calculated, the values of γ_n are determined, and the diffusivity D_s is optimized through nonlinear least squares fitting. Figure S4 presents the fit obtained for the kinetics at 40 ppm and 25 °C.

Based on the results obtained (Figure S4), it appears that although intraparticle diffusion plays a significant role, both stages (3 and 4) are involved in the adsorption process, without ruling out the possibility that intraparticle diffusion is the rate-controlling step.

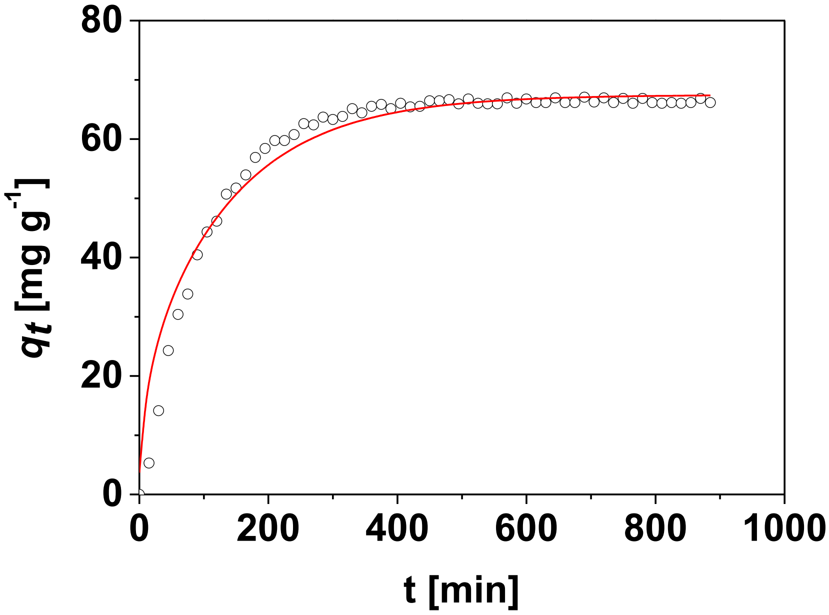

Figure S4: Crank's intraparticle diffusion model applied to the kinetics at 40 ppm and 25°C.

b2) Single Resistance Model: Diffusion Through the External Film

Considering a finite volume, Equation (2) and a linear isotherm ($q_e = KC_e$), — where C_i is in equilibrium with q just as C_e is with q_e —allow substitution of C_t and C_i in Equation (6) in terms of C_o and q_t, resulting in Equation (11), which can be integrated to yield Equation (12).

$$\frac{dq_t}{dt} = k_f S_A \left(C_o - q_t \left(\frac{M}{V} + \frac{1}{K} \right) \right) \quad (11)$$

$$\frac{q_t}{q_e} = 1 - \exp\left(-k_f S_A \left(\frac{MK + V}{VK} \right) t \right) \quad (12)$$

The exponential term in Equation (12) remains constant for any given set of experimental data and is equivalent to Equation (4). Figure S5 displays the fit obtained for the kinetics at 40 ppm and 25 °C, and shows that the model fits the experimental data correctly. However, intraparticle diffusion cannot be ruled out, making it necessary to develop a dual-resistance model to determine which of the two mechanisms predominates.

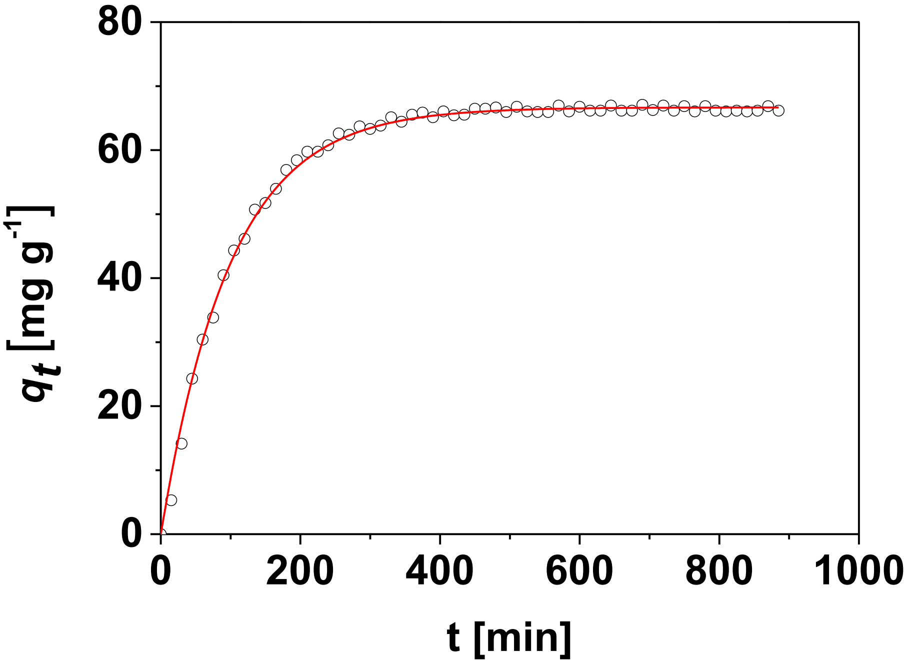

Figure S5: Crank model of external film diffusion applied to the kinetics at 40 ppm and 25°C.

b3) Dual-Resistance Model: Diffusion Through the External Film and Intraparticle Diffusion

Crank[2] derived the model analytically, providing a more realistic solution that incorporates both diffusion mechanisms, as expressed in Equation (13).

$$\frac{q_t}{q_e} = 1 - \sum_{n=1}^{\infty} \frac{2B_i^2 exp(-\beta_n^2 D_s t/l^2)}{\beta_n^2(\beta_n^2 + B_i^2 + B_i)} \qquad (13)$$

Where β_n are the positive roots of:

$$\beta_n tan\beta_n = B_i \qquad (14)$$

The parameter B_i depends, in turn, on k_f, D_S y l, as described by Equation (15).

$$B_i = \frac{k_f l}{D_s} \qquad (15)$$

Using Equations (13) to (15) and the Origin software, the parameters D_s y k_f were optimized through nonlinear least squares fitting. Figure S6 presents the results obtained for the kinetics at 40 ppm and 25 °C. This model, applied to spherical particles, has been employed by other researchers (Chatterjee and Schiewer, 2014; Choy and McKay, 2005; Topp and Pepper, 1949).

This model (Figure 3a, manuscript), provides the best fit, confirming that both diffusion processes contribute to the adsorption reaction. Table S4 presents the parameters obtained from fitting using Equation (13).

Table S4: Parameters Obtained by Nonlinear Least Squares Fitting to Equation (13)

C_o [ppm]	D_s 10^4 [cm^2 min^{-1}]	k_f 10^4 [cm min^{-1}]	q_e [mg g^{-1}]	B_i	R^2
103 ± 1	1.33 ± 0.07	1.49 ± 0.05	123.4 ± 0.5	0.0099 ± 0.0005	0.9939
91 ± 3	1.18 ± 0.06	1.32 ± 0.08	120 ± 3	0.0095 ± 0.0006	0.9945
82 ± 2	1.11 ± 0.05	1.30 ± 0.04	110 ± 3	0.0101 ± 0.0005	0.9947
73 ± 1	1.15 ± 0.03	1.27 ± 0.06	105 ± 7	0.0097 ± 0.0004	0.9966
60 ± 2	1.07 ± 0.01	1.24 ± 0.04	94.5 ± 0.3	0.0094 ± 0.0005	0.9935
53 ± 1	1.1 ± 0.2	1.2 ± 0.2	85.2 ± 0.5	0.0097 ± 0.0003	0.9970
41 ± 1	1.0 ± 0.2	1.1 ± 0.2	68 ± 2	0.0096 ± 0.0003	0.9971
31 ± 2	1.0 ± 0.1	1.1 ± 0.1	51 ± 4	0.0098 ± 0.0003	0.9960
20 ± 1	0.91 ± 0.05	0.96 ± 0.04	32.7 ± 0.2	0.0092 ± 0.0004	0.9942
9 ± 1	0.89 ± 0.06	0.91 ± 0.04	16.6 ± 0.1	0.0089 ± 0.0006	0.9913
4 ± 1	0.8 ± 0.2	0.9 ± 0.3	7.21 ± 0.07	0.0093 ± 0.0005	0.9924

Once the external and internal diffusion coefficients have been determined for the different concentrations, the rate-limiting step can be assessed in terms of the Biot number, B_i,, which relates the external mass transfer resistance to the internal mass transfer resistance, as defined in Equation (15). When $B_i >> 1$,, the adsorption process is primarily controlled by intraparticle diffusion; conversely, when $B_i << 1$, external diffusion predominantly governs the rate (Choy and McKay, 2005; Dávila-Guzman et al., 2012; Illanes et al., 2008). Based on the B_i values presented in Table 1, it is concluded that the main rate-controlling step in this adsorption process is diffusion across the boundary layer, i.e., external mass transfer (Stage 2).

Weber and Chakkravorti define the dimensionless constant known as the separation factor or equilibrium parameter, R_L (Equation 16) (Weber and Chakravorti, 1974), which characterizes the shape of the adsorption isotherm. When the values of R_L lie between 0 and 1, as shown in Figure S6, the adsorption of the adsorbate onto the surface of the adsorbent is considered favorable under the given operating conditions

$$R_L = \frac{1}{1+K_L C_o} \qquad (16)$$

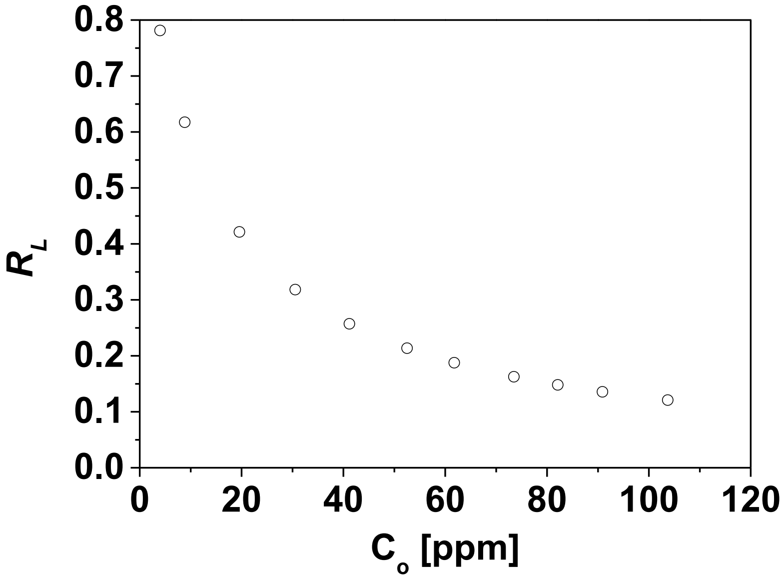

Figure S6: Effect of initial concentration on the equilibrium parameter

References

Azizian, S., 2004. Kinetic models of sorption: A theoretical analysis. *J. Colloid Interface Sci.* **276**, 47–52. https://doi.org/10.1016/j.jcis.2004.03.048

Chatterjee, A., Schiewer, S., 2014. Multi-resistance kinetic models for biosorption of Cd by raw and immobilized citrus peels in batch and packed-bed columns. *Chem. Eng. J.* **244**, 105–116. https://doi.org/10.1016/j.cej.2013.12.017

Choy, K.K.H., McKay, G., 2005. Sorption of cadmium, copper, and zinc ions onto bone char using Crank diffusion model. *Chemosphere* **60**, 1141–1150. https://doi.org/10.1016/j.chemosphere.2004.12.041

Crank, J., 1979. *The Mathematics of Diffusion.*, second ed. Oxford University Press, Oxford.

Dávila-Guzmán, N.E., Cerino-Córdova, F.J., Díaz-Flores, P.E., Rangel-Méndez, J.R., Sánchez-González, M.N., Soto-Regalado, E., 2012. Equilibrium and kinetic studies of ferulic acid adsorption by Amberlite XAD-16. *Chem. Eng. J.* **183**, 112–116. https://doi.org/10.1016/j.cej.2011.12.037

Illanes, C.O., Ochoa, N.A., Marchese, J., 2008. Kinetic sorption of Cr(VI) into solvent impregnated porous microspheres. *Chem. Eng. J.* **136**, 92–98. https://doi.org/10.1016/j.cej.2007.03.008

Topp, N.E., Pepper, K.W., 1949. Properties of ion-exchange resins in relation to their structure. Part I. Titration curves. *J. Chem. Soc.* **2836**, 3299–3303. https://doi.org/10.1039/jr9490003299

Weber, T.W., Chakravorti, R.K., 1974. Pore and solid diffusion models for fixed-bed adsorbers. *AIChE J.* **20**, 228–238. https://doi.org/10.1002/aic.690200204